

12

AD-A275 213



The Pennsylvania State University
APPLIED RESEARCH LABORATORY
P.O. Box 30
State College, PA 16804

**UNCERTAINTY PRODUCT SCATTERING
FUNCTION ESTIMATION**

by

M. J. Gustafson
D. W. Ricker

Technical Report No. TR 94-01
January 1994

DTIC
ELECTE
JAN 31 1994
S E D

Supported by:
Office of Naval Research

L.R. Hettche, Director
Applied Research Laboratory

Approved for public release; distribution unlimited

94 1 28 055

116P

94-02918



REPORT DOCUMENTATION PAGE

Form Approved
OMB No. 0704-0160

Public reporting burden for the collection of information is estimated to average 1 hour per response, including the time for reviewing instructions, searching existing data sources, gathering and maintaining the data needed, and completing and reviewing the collection of information. Send comments regarding this burden estimate or any other aspect of the collection of information, including suggestions for reducing the burden, to Washington Headquarters Services, Directorate for Information Operations and Reports, 1215 Jefferson Davis Highway, Suite 1204, Arlington, VA 22202-4302, and to the Office of Management and Budget, Paperwork Reduction Project 0704-0160, Washington, DC 20503.

| | | | |
|--|--|---|--|
| 1. AGENCY USE ONLY (Leave blank) | 2. REPORT DATE | 3. REPORT TYPE AND DATES COVERED | |
| | January 1994 | Technical Report - Final | |
| 4. TITLE AND SUBTITLE | | | 5. FUNDING NUMBERS |
| Uncertainty Product Scattering Function Estimation | | | N00039-92-C-0100 |
| 6. AUTHOR(S) | | | |
| Michael J. Gustafson | | | |
| 7. PERFORMING ORGANIZATION NAME(S) AND ADDRESS(ES) | | | 8. PERFORMING ORGANIZATION REPORT NUMBER |
| Applied Research Laboratory The Pennsylvania State University P. O. Box 30 State College, PA 16804 | | | TR-94-01 |
| 9. SPONSORING/MONITORING AGENCY NAME(S) AND ADDRESS(ES) | | | 10. SPONSORING/MONITORING AGENCY REPORT NUMBER |
| Office of Naval Research Ballston Tower 1 800 N. Quincy Street Arlington, VA 22217-5660 | | | |
| 11. SUPPLEMENTARY NOTES | | | |
| 12a. DISTRIBUTION/AVAILABILITY STATEMENT | | | 12b. DISTRIBUTION CODE |
| Distribution Statement A: Approved for public release; Distribution is unlimited. | | | |
| 13. ABSTRACT (Maximum 200 words) | | | |
| <p>A new concept for the estimation of scattering processes in the delay-Doppler (phase) plane has been proposed [1,2]. It reduces ambiguity self-clutter effects by forming a test statistic from the product of two auto-uncertainty functions generated by the transmission of two separate waveforms. These must be transmitted in close temporal proximity yet should be disjoint in the sense that their cross-uncertainty function is required to have minimal support close to the origin. Initial results indicate that the technique produces much cleaner estimates of the scattering process with much less of the sidelobe effect normally experienced with large TW signals.</p> | | | |
| 14. SUBJECT TERMS | | | 15. NUMBER OF PAGES |
| | | | 107 |
| | | | 16. PRICE CODE |
| 17. SECURITY CLASSIFICATION OF REPORT | 18. SECURITY CLASSIFICATION OF THIS PAGE | 19. SECURITY CLASSIFICATION OF ABSTRACT | 20. LIMITATION OF ABSTRACT |
| UNCLASSIFIED | UNCLASSIFIED | UNCLASSIFIED | UL |

Acknowledgements

The authors wish to thank Peter Dahl of the Applied Physics Laboratory/University of Washington for supplying the FLIP surface scattering data and information on test conditions.

This work was supported by the Office of Naval Research under COMSPAWARSCOM contract N000-39-92-C-0100.

| | |
|----------------------|---|
| Accesion For | |
| NTIS | CRA&I <input checked="" type="checkbox"/> |
| DTIC | TAB <input type="checkbox"/> |
| U. announced | <input type="checkbox"/> |
| J. publication | |
| By | |
| Distrib. to .. / | |
| Availability Codes | |
| Dist | Avail and / or Special |
| A-1 | |

DTIC QUALITY INSPECTED 2

Table of Contents

| | |
|--|-----------|
| List of Figures | vi |
| List of Tables | ix |
| Acknowledgements | x |
| Chapter 1 Introduction | 1 |
| 1.1 Motivation | 1 |
| 1.2 Thesis Outline | 3 |
| Chapter 2 Matched Filter and Ambiguity Theory | 6 |
| 2.1 The Channel Model | 6 |
| 2.2 The Matched Filter Receiver | 10 |
| 2.3 Ambiguity Function Properties and Signal Resolution | 13 |
| Chapter 3 The Uncertainty Product (UP) Receiver | 21 |
| 3.1 UP Receiver Structure | 21 |
| 3.2 UPF Properties | 27 |
| 3.2.1 Relationship to the Cross-Ambiguity Function | 27 |
| 3.2.2 UPF Volume | 28 |
| 3.2.3 Maximum Value | 29 |
| Chapter 4 Implementation Issues | 31 |
| 4.1 Disjoint Waveform Support | 31 |
| 4.2 Simultaneous Observability | 39 |
| 4.3 Virtual Scattering | 42 |
| Chapter 5 Waveform Design Considerations | 53 |
| 5.1 Component Waveforms | 54 |
| 5.1.1 The CW | 54 |
| 5.1.2 The Linear FM | 55 |
| 5.1.3 Frequency Hop-Coded Waveforms | 58 |
| 5.2 The Product of Hit Arrays | 67 |
| 5.3 Code Density | 70 |
| 5.4 Application Specific Design | 75 |
| Chapter 6 Open Ocean Surface Scattering Function Estimation | 79 |
| 6.1 Experiment Overview | 79 |
| 6.2 Waveform Selection | 82 |
| 6.3 Forward Scattering Function Estimation | 83 |
| 6.3.1 Receiver Modifications | 83 |

| | | |
|---|---|-----|
| 6.3.2 | Phase Plane Motion | 89 |
| 6.3.3 | Uncertainty Product Receiver Processing | 92 |
| 6.3.4 | Receiver Performance | 97 |
| Chapter 7 Summary and Conclusions | | 102 |
| References | | 105 |

List of Figures

| | | |
|-----|---|----|
| 2.1 | The Linear, Time-varying, Random Channel Model | 7 |
| 2.2 | The Matched Filter Receiver | 11 |
| 2.3 | CW Ambiguity Function | 16 |
| 2.4 | Generic Costas Ambiguity Function | 18 |
| 2.5 | Sample Matched Filter Output | 20 |
| 3.1 | The UP Receiver | 22 |
| 3.2 | Sample Cross-Ambiguity Function | 25 |
| 3.3 | Sample Uncertainty Product Function | 26 |
| 4.1 | Disjoint Waveform Support | 35 |
| 4.2 | The Disjoint V-chirp Waveform | 36 |
| 4.3 | Disjoint V-chirp Output for l_g | 38 |
| 4.4 | UP Receiver Waveforms | 43 |
| 4.5 | UP Receiver Output for a Deterministic Scattering Function | 45 |
| 4.6 | Uncertainty Function Interaction | 46 |
| 4.7 | UP Receiver Output for N Realizations: (a) N = 1, (b) N = 10, (c) N = 100, (d) N = 300 | 49 |
| 4.8 | Matched Filter Output for N Realizations: (a) N = 1, (b) N = 10, (c) N = 100, (d) N = 300 | 51 |
| 4.9 | Receiver Background Comparison | 52 |
| 5.1 | Hamming Windowed CW Pulse | 56 |
| 5.2 | Sample Linear FM | 57 |

| | | |
|------|--|----|
| 5.3 | Disjoint V-chirp UPF with Rectangular Window | 59 |
| 5.4 | Sample Time-Frequency Pattern | 61 |
| 5.5 | Time-Frequency Auto-correlation Pattern | 62 |
| 5.6 | Sample Costas Ambiguity Function | 64 |
| 5.7 | Sample Time-Frequency Patterns of Various Constructions | 66 |
| 5.8 | Hit Array Analysis for Up/Down SteppedLFMs | 69 |
| 5.9 | Hit Array Analysis for Up/Down SteppedLFMs | 72 |
| 5.10 | High Density Hop Code Ambiguity Function | 74 |
| 5.11 | Golomb Time-Frequency Pattern and Associated Auto-Hit Array . | 76 |
| 6.1 | FLIP Forward Scattering Geometry | 80 |
| 6.2 | FLIP Vertical Receive Beam Pattern | 81 |
| 6.3 | FLIP Waveform Time-Frequency Patterns | 84 |
| 6.4 | FLIP Waveform Functions: (a) Waveform 1 Ambiguity Function, (b) Uncertainty Product Function | 85 |
| 6.5 | FLIP Ping 1 Time Series and Spectrum | 86 |
| 6.6 | FLIP Truncated Waveform Functions: (a) Waveform 1 Ambiguity Function, (b) Uncertainty Product Function | 88 |
| 6.7 | FLIP Ping 1 First Channel Matched Filter Output | 90 |
| 6.8 | Direct Path Range and Doppler Positions | 91 |
| 6.9 | FLIP Uncertainty Product Function Contour Map | 93 |
| 6.10 | FLIP Uncertainty Product 24 Ping Ensemble Average | 94 |
| 6.11 | Direct Path Reregistered Uncertainty Product Receiver Ensemble Average | 95 |

| | |
|---|-----|
| 6.12 Surface Path Reregistered Uncertainty Product Receiver Ensemble Average | 98 |
| 6.13 Receiver Ensemble Average Contour Maps | 100 |
| 6.14 Receiver Convergence Comparison | 101 |

List of Tables

| | | |
|-----|---|----|
| 5.1 | Welch Construction Minimum Hit Array Pairs | 71 |
| 5.2 | HC Construction Minimum Hit Array Pairs | 71 |
| 5.3 | Golomb Construction Minimum Hit Array Pairs | 72 |

Chapter 1

Introduction

1.1 Motivation

Much effort has been devoted to the problem of estimating the structure of underwater acoustic communication channels and scattering phenomena in the ocean medium. These channels are often modeled as linear, time-variant, space-variant, random filters [3]. Transmitted acoustic signals often experience spreading in both time and frequency as they pass through the channel. Time delay spread is induced by the motion of the source and/or receiver, the ocean boundaries (multipath), and various other acoustic scatterers throughout the medium. Frequency spreading is introduced by the motion of scatterers in the medium and by motion of the volume and surface [4]. Underwater acoustic systems have the added problem of interference from reverberation backscattered from the bottom, surface, and ocean volume.

In many electromagnetic and acoustic applications, the scattering function can be used to represent the average distribution of scattered energy in the delay-Doppler (phase) plane. A scattering function may be estimated using active interrogation and conventional (narrowband) matched filter processing if the energy in each resolution cell at the output of the receiver is averaged over multiple

interrogations. The average distribution may, under wide sense stationary and uncorrelated spreading (WSSUS) conditions, be considered as a convolution of the signal ambiguity function and the scattering function [5, 6]. The accuracy of the estimate is increased when the ambiguity function approaches a two-dimensional Dirac delta or "thumbtack" function. Although much effort has gone into the design of waveforms which approximate this ideal form, limits are imposed on mainlobe resolution and sidelobe flatness by the ambiguity function's volume conservation property. Since volume is conserved in the ambiguity function, most of the phase plane energy is the result of the convolution of the pedestal and base portions with the scattering function, which has the potential to obscure the high resolution mainlobe contribution especially in the presence of dense scattering.

Mehta and Titlebaum [1, 2] have proposed a new twin processor receiver structure which does not have the limitations of the traditional matched filter receiver. This new method involves passing two waveforms through the channel separately and processing each with its own correlation receiver. The complex outputs of each of these receivers are then multiplied (with one channel first conjugated) to form a statistic for estimation of the underlying scattering process. As with the matched filter, the expected value of this receiver is also written as a convolution, with the scattering function as the kernel. However, in this case, the convolution is with the product of the two waveform auto-uncertainty functions which we will refer to as the uncertainty product function (UPF)¹. The UPF does not have the

¹Because of this convolution property, for the remainder of this thesis we shall refer to the

volume conservation constraints of the ambiguity function, implying that the twin processor (or uncertainty product) receiver is capable of producing better estimates of the scattering process in the presence of additive noise.

This thesis presents a detailed discussion of the uncertainty product receiver and derives an expression for the rate of the convergence of the receiver to its expected value. In addition, several properties of the uncertainty product function are derived and used to characterize receiver performance and motivate signal design criteria. Both simulated and in-water data are used to measure convergence rates and to demonstrate improved performance as compared to the matched filter receiver.

1.2 Thesis Outline

In Chapter 2, the acoustic channel is modeled as a linear, time-varying, random filter with additive noise. In this model, the spreading function is used to describe the time and frequency spreading characteristics of the channel. Under WSSUS assumptions, the expected output of the narrowband matched filter is shown to be equal to the convolution of the channel scattering function and the signal ambiguity function. Properties of the ambiguity function are presented to explain the performance limits of the matched filter receiver and to provide a comparison with the properties of the UPF in the following chapter.

Chapter 3 presents the uncertainty product receiver whose twin processor

twin processor structure as the uncertainty product (UP) receiver.

structure was originally proposed by Mehta and Titlebaum [1]. The uncertainty product function (UPF) is then defined, and the expected output of the UP receiver is shown to be equal to the convolution of the UPF with the system scattering function. Several properties of the UPF are derived, including the UPF's lack of conservation of volume and relationship to the two waveforms' cross-ambiguity function. These properties are compared to those of the ambiguity function to illustrate the improved performance of the UP receiver over that of the traditional narrowband matched filter.

Several problems arise when two waveforms are used to interrogate the channel during a single transmission cycle. Interaction of the UP receiver's constituent waveforms is discussed in Chapter 4. Requirements for time and frequency separation of the two waveforms are developed which ensure that each signal interrogates the same realization of the scattering process, while minimizing the adverse effects introduced by their cross-ambiguity function. Also, the problem of "virtual scattering" is described. "Virtual scatterers" are spurious peaks which occur in the range-Doppler plane due to the interaction of the two uncertainty functions in the presence of two or more point scatterers. These peaks are shown to disappear as the expected value of the UP receiver is reached. A theoretical prediction of the rate of decay is derived for the virtual scattering process and confirmed using computer simulation.

Chapter 5 presents an overview of various waveform constructions and their associated ambiguity functions. Waveforms discussed include CWs,LFMs, and fre-

quency hop codes of commonly used algebraic constructions. Next, the hit array [7] is introduced as a geometric tool for measuring mainlobe and sidelobe structure in waveform auto- and cross-ambiguity functions of frequency hop codes. In addition, it is shown that the product of the two waveform auto-hit arrays can, under certain conditions, be used to approximate the UPF structure. Recommendations are given for selecting maximally resolvent and minimally interfering waveforms.

Chapter 6 presents the results of using the UP receiver to measure the ocean direct path and surface scattering mechanisms. The experiment, conducted off the coast of California, employed a bistatic sonar to measure direct-path and surface reflected-path propagation. The average output of the UP receiver is shown to produce lower sidelobe levels than those of the narrowband matched filter formed using one of the waveforms alone. In addition, a physical interpretation of the channel scattering function estimate is given.

Chapter 2

Matched Filter and Ambiguity Theory

2.1 The Channel Model

As previously mentioned, it is often desirable to model the underwater acoustic channel as a time-varying, linear, random filter. Using this model, linear system theory methods may be used to predict the average response of the channel due to any input signal. The relationship between the output of the channel, $r(t)$, due to an arbitrary input signal, $x(t)$, is given by the *time-varying impulse response*, $h(\tau, t)$, which describes the response of the filter at time t due to the application of unit impulse at time $(t - \tau)$. In general, $h(\tau, t)$ is modeled as a random function to account for the variations in the ocean medium which may be considered stochastic in nature. As in this case, all other system functions developed here will be considered to be random functions and their expected values will be used to describe the output of the channel.

If the waveform transmitted into the acoustic medium is given by $x(t)$ and the channel output is given by $r(t)$, the channel may be described by the linear filter shown in Figure 2.1. The standard I/O relationship for this linear system is given by [8]

$$r(t) = \sqrt{E_x} \int_{-\infty}^{+\infty} x(t - \tau) h(\tau, t) d\tau + n(t), \quad (2.1)$$

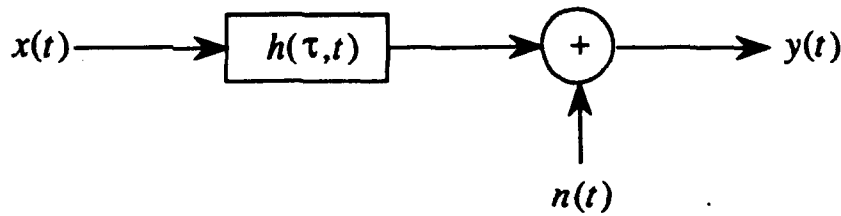


Figure 2.1: The Linear, Time-varying, Random Channel Model

where E_x is the energy contained in the transmitted signal and $n(t)$ represents the additive noise present in the channel. This noise term will temporarily be dropped in order to study the effects of the impulse response, $h(\tau, t)$, alone.

In [3] it is shown that the channel characteristics may also be described in the frequency domain using the *time-varying channel transfer function* $H(f, t)$ which is defined as the Fourier transform of $h(\tau, t)$ w. r. t. τ , and is given by [8]

$$H(f, t) = \int_{-\infty}^{+\infty} h(\tau, t) e^{-j2\pi f \tau} d\tau \quad (2.2)$$

where $H(f, t)$ is a function of both time and the input frequencies, f , in Hertz. The relationship in the frequency domain can be shown to be

$$r(t) = \sqrt{E_x} \int_{-\infty}^{+\infty} X(f) H(f, t) e^{j2\pi f t} df \quad (2.3)$$

which implies that $H(f, t)$ describes the amplitude scaling and phase shift which

the input signal spectrum undergoes over time.

Following a similar development, Ziomek [3] describes the frequency domain response of the system using the *spreading function* $S(\tau, \phi)$ and the *bi-frequency function* $B(f, \phi)$ which are defined as the Fourier transforms of $h(\tau, t)$ and $H(f, t)$ with respect to the time variable t ,

$$S(\tau, \phi) = \int_{-\infty}^{+\infty} h(\tau, t) e^{-j2\pi\phi t} dt \quad (2.4)$$

and

$$B(f, \phi) = \int_{-\infty}^{+\infty} H(f, t) e^{-j2\pi\phi t} dt. \quad (2.5)$$

Fourier transform relationships can be established between any of these four system functions and used to show that each of these functions provides an equivalent description of the channel time and frequency spreading characteristics. As per common practice [9], we shall use the system spreading function $S(\tau, \phi)$ to describe the channel and determine the expected output of the system.

From (2.4), $h(\tau, t)$ may be written as

$$h(\tau, t) = F_{\phi}^{-1}\{S(\tau, \phi)\} \quad (2.6)$$

where $F_{\phi}^{-1}\{\cdot\}$ denotes the inverse Fourier transform of the function w. r. t. the frequency variable ϕ . Using (2.1) and (2.6), the output of the filter may be written

in terms of the spreading function as

$$r(t) = \sqrt{E_x} \int_{-\infty}^{+\infty} x(t-\tau) e^{j2\pi\phi\tau} S(\tau, \phi) d\tau d\phi + n(t). \quad (2.7)$$

Equation (2.7) states that the channel output, $r(t)$, can be represented by the sum of time and frequency shifted replicas of the transmit signal weighted by the spreading function, plus additive noise. Thus, the spreading function is shown to be a description of the time and frequency spreading characteristics of the channel for one realization of the filter.

Ziomek [3] introduces the auto-correlation functions $R_h(\tau, \tau', t, t')$, $R_H(f, f', t, t')$, $R_S(\tau, \tau', \phi, \phi')$, and $R_B(f, f', \phi, \phi')$ to describe the characteristics of the four system functions over time. As with the system functions, Fourier transform relationships can be developed between the four auto-correlation functions. These relationships may then be used to show that wide sense stationarity in time is equivalent to uncorrelated spreading in frequency and that wide sense stationarity in frequency is equivalent to uncorrelated spreading in time. When both of the situations occur, the acoustic channel is said to be Wide Sense Stationary Uncorrelated Spreading (WSSUS) and the system auto-correlation functions may each be reduced to functions of two variables.

The auto-correlation function of the system spreading function may be used to describe the average properties of the stochastic channel over time. In general

this function is given by

$$R_S(\tau, \tau', \phi, \phi') = E\{S(\tau, \phi)S^*(\tau', \phi')\}. \quad (2.8)$$

If a WSSUS channel is assumed, i. e. the spreading function is uncorrelated for all $\tau \neq \tau'$ and $\phi \neq \phi'$, then the auto-correlation function becomes

$$R_S(\tau, \tau', \phi, \phi') = E\{|S(\tau, \phi)|^2\}\delta(\tau - \tau')\delta(\phi - \phi') \quad (2.9)$$

$$\equiv R_S(\tau, \phi)\delta(\tau - \tau')\delta(\phi - \phi'). \quad (2.10)$$

The term $R_S(\tau, \phi)$ is referred to as the system scattering function and is a measure of how the medium redistributes the transmitted signal energy, E_x , in range delay, τ , and Doppler shift, ϕ [9]. The scattering function is the most commonly used narrowband characterization of the underwater communications channel and may be used to optimize performance of active echo location systems [10].

2.2 The Matched Filter Receiver

The matched filter is the optimum receiver for a slowly fluctuating point reflector in the presence of white Gaussian noise[6]. The structure of the receiver is shown in Figure 2.2 and is given by [3]

$$|l(\hat{\tau}, \hat{\phi})|^2 = \left| \int_{-\infty}^{+\infty} r(t)x^*(t - \hat{\tau})e^{-j2\pi\hat{\phi}t} dt \right|^2 \quad (2.11)$$

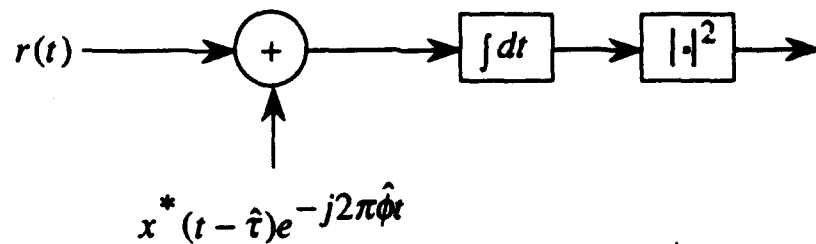


Figure 2.2: The Matched Filter Receiver

where $\hat{\tau}$ is the hypothesized range delay, $\hat{\phi}$ is the hypothesized frequency shift, $r(t)$ is the received signal as given by (2.1), and $x(t)$ is the transmitted waveform.

If we temporarily disregard the noise term, $n(t)$, and express the channel output $r(t)$ in terms of the spreading function of (2.4), the output of the receiver may be written as

$$|l(\hat{\tau}, \hat{\phi})|^2 = \left| \int_{-\infty}^{+\infty} \int_{-\infty}^{+\infty} S(\tau, \phi) e^{j2\pi\Delta\phi\tau} \chi_{xx}(\Delta\tau, \Delta\phi) d\tau d\phi \right|^2 \quad (2.12)$$

where

$$\Delta\tau \equiv \tau - \hat{\tau} \quad (2.13)$$

and

$$\Delta\phi \equiv \phi - \hat{\phi}. \quad (2.14)$$

In Equation (2.12), $\chi_{xx}(\Delta\tau, \Delta\phi)$ represents the transmit signal *auto-uncertainty*

function[11]

$$\chi_{xx}(\Delta\tau, \Delta\phi) = \int_{-\infty}^{+\infty} x(t - \Delta\tau - \hat{\tau}) x^*(t - \tau + \Delta\tau) e^{-j2\pi\Delta\phi t} dt. \quad (2.15)$$

One stochastic realization of the matched filter is given by $|l(\hat{\tau}, \hat{\phi})|^2$. The expected output of the matched filter provides a probabilistic description of the fluctuating channel. If a WSSUS communication channel is assumed, the expected output of the matched filter is given by [11]

$$\begin{aligned} m(\hat{\tau}, \hat{\phi}) &= E\{|l(\hat{\tau}, \hat{\phi})|^2\} \\ &= \int_{-\infty}^{+\infty} \int_{-\infty}^{+\infty} R_S(\tau, \phi) |\chi_{xx}(\Delta\tau, \Delta\phi)|^2 d\tau d\phi + N_0 \end{aligned} \quad (2.16)$$

where $R_S(\tau, \phi)$ is the system scattering function of Equation (2.10) (arising from the assumption of uncorrelated spreading), $|\chi_{xx}(\Delta\tau, \Delta\phi)|^2$ is referred to as the transmit signal *auto-ambiguity function* and is the magnitude-squared of the auto-uncertainty function of (2.15), and N_0 is the noise spectral density. The matched filter output $m(\hat{\tau}, \hat{\phi})$ is generally computed over a region of hypothesized time delays $\hat{\tau}$ and frequency shifts $\hat{\phi}$ corresponding to the region of support of the scattering function in the phase plane.

Equation (2.16) shows that the expected output of the matched filter is the two-dimensional convolution of the system scattering function with the signal ambiguity function. If the objective is to estimate the scattering function, the ideal choice for a transmit waveform would be one which has an ambiguity function of

the form

$$|\chi_{xx}(\Delta\tau, \Delta\phi)|^2 = \delta(\Delta\tau)\delta(\Delta\phi) \quad (2.17)$$

which describes a two-dimensional Dirac delta function, or "spike", with support only at the origin, where $\tau = \hat{\tau}$ and $\phi = \hat{\phi}$. This would produce the matched filter output

$$m(\hat{\tau}, \hat{\phi}) = E_x R_S(\hat{\tau}, \hat{\phi}) + N_0 \quad (2.18)$$

yielding a perfect measurement of the scattering function, except for the addition of corruptive noise. Unfortunately, this idealized result is not exactly obtainable due to ambiguity function properties.

2.3 Ambiguity Function Properties and Signal Resolution

Considerable effort has gone into the design of waveforms yielding ambiguity surfaces which approximate the ideal form described in (2.17). Properties of the ambiguity function will be introduced, and bounds on resolution may be derived which influence the matched filter scattering function estimate.

Using the auto-uncertainty function in Equation (2.15), the signal auto-ambiguity function is given by

$$|\chi_{xx}(\Delta\tau, \Delta\phi)|^2 = \left| \int_{-\infty}^{+\infty} x(t)x^*(t - \Delta\tau)e^{-j2\pi\Delta\phi t} dt \right|^2. \quad (2.19)$$

Using this equation, several properties may be described [11]:

1. **Maximum value.** The Schwarz inequality can be used to show that

$$|\chi(\Delta\tau, \Delta\phi)|^2 \leq \left| \int_{-\infty}^{+\infty} |x(t)|^2 dt \right|^2 = |\chi(0, 0)|^2. \quad (2.20)$$

We can normalize the signal $x(t)$ so that

$$|\chi(0, 0)|^2 = 1. \quad (2.21)$$

2. **Symmetry about the origin.**

$$|\chi_{xx}(-\Delta\tau, -\Delta\phi)|^2 = |\chi_{xx}(\Delta\tau, \Delta\phi)|^2. \quad (2.22)$$

3. **Self Transform.** The ambiguity function is identical to its two-dimensional Fourier transform

$$\int_{-\infty}^{+\infty} \int_{-\infty}^{+\infty} |\chi_{xx}(\tau, \phi)|^2 e^{j2\pi(\tau\nu - \phi u)} d\tau d\phi = |\chi_{xx}(\nu, u)|^2. \quad (2.23)$$

4. **Volume invariance.** The total volume contained under the ambiguity function is constant regardless of the normalized signal, i. e.

$$\int_{-\infty}^{+\infty} \int_{-\infty}^{+\infty} |\chi(\tau, \phi)|^2 d\tau d\phi = |\chi(0, 0)|^2 = 1. \quad (2.24)$$

This property, which is known as the **radar uncertainty principle**, is

probably the most important property of the ambiguity function. Clearly, if a signal is designed such that its ambiguity function mainlobe approaches a delta function, then (2.24) demands that the volume removed from the mainlobe will appear elsewhere in the $\tau\phi$ plane, affecting receiver performance. A more detailed discussion of the effects of this result will be given shortly.

Throughout this discussion, T will denote the transmit signal duration in seconds and W will denote the signal bandwidth in Hertz. In general, the signal resolution (defined by the 3 dB contour on the ambiguity function mainlobe) is proportional to $1/W$ in delay and $1/T$ in Doppler[11]. A signal often used in scattering function identification is the CW (or pure tone) whose ambiguity function is shown in Figure 2.3. The CW has the property that its bandwidth is equal to the inverse of its duration, so that $TW = T(1/T) = 1$, implying that this type of signal may be resolvent in Doppler (as in Figure 2.3) or in range depending on the pulse length, but not both.

As a result of the radar uncertainty principle, any realizable ambiguity function will consist of a centralized "spike" or mainlobe and a distributed volume "pedestal" or sidelobe region about the mainlobe. The ideal ambiguity function is one with a very narrow mainlobe and completely flat sidelobes, which is commonly referred to as the "thumbtack" ambiguity function[11].

In the past, a great deal of work has gone into the design of waveforms which approximate the "thumbtack" form. More recently, the majority of this work has

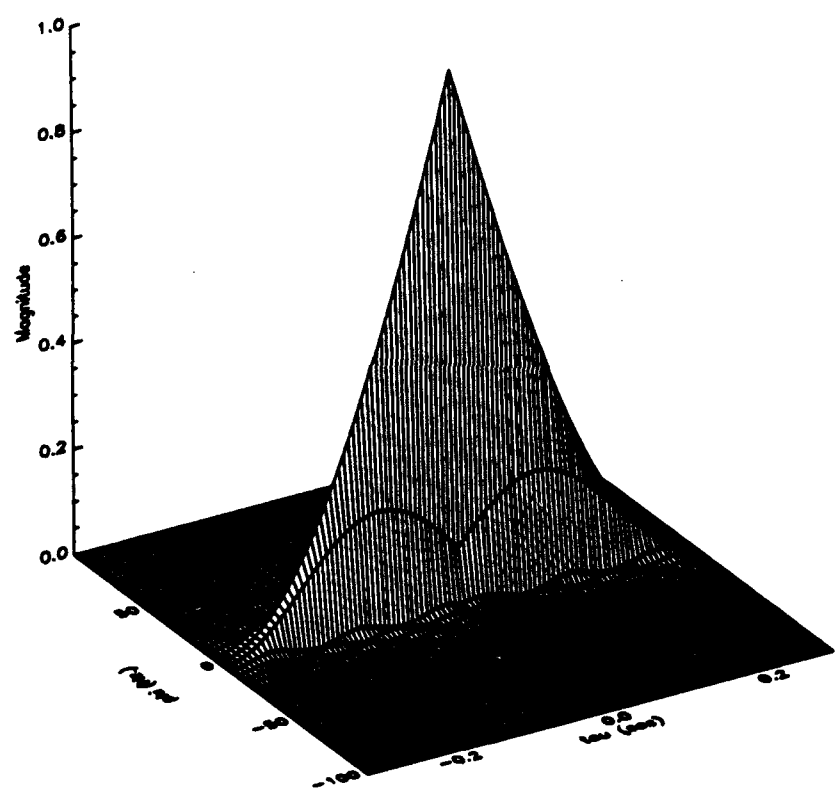


Figure 2.3: CW Ambiguity Function

been directed toward the study of time-frequency hop (hop code) signals. These signals, which are also referred to as frequency shift keyed (FSK) signals, consist of a set of CW subpulses concatenated in time, each at a separate frequency.

A class of FSK codes originally introduced by Costas [12] has the desirable properties of a delta-like mainlobe and a relatively flat sidelobe region. Such signals may be designed with an arbitrarily large duration and bandwidth, yielding high resolution in both delay and Doppler. However, increasing the code TW product tends to decrease the volume of the mainlobe. Because ambiguity volume is conserved, volume removed from the main lobe is distributed to the sidelobe region where it contributes to "self-clutter". Self-clutter arises when multiple, dense scattering exists, causing the receiver response at a particular delay-Doppler hypothesis to contain contributions from scattering sites throughout the plane. These spurious contributions represent energy integrated by the sidelobe pedestal and base regions which surround the main lobe as illustrated by the idealized ambiguity function shown in Figure 2.4. In the figure, a unit energy code of order N subpulses with a total duration of T seconds and bandwidth W is assumed. The bandwidth is related to N and T through the assumption that the subpulses are separated in frequency by their spectral width N/T [13]. The base of the ambiguity function is a result of interpulse ambiguity interaction and is of height $1/N^2$ since Costas codes by design can only generate "single hit" subpulse correlations [14]. The pedestal region surrounding the main lobe is dominated by the incoherent addition of the subpulse spectral sidelobes and has a average height of $1/N$.

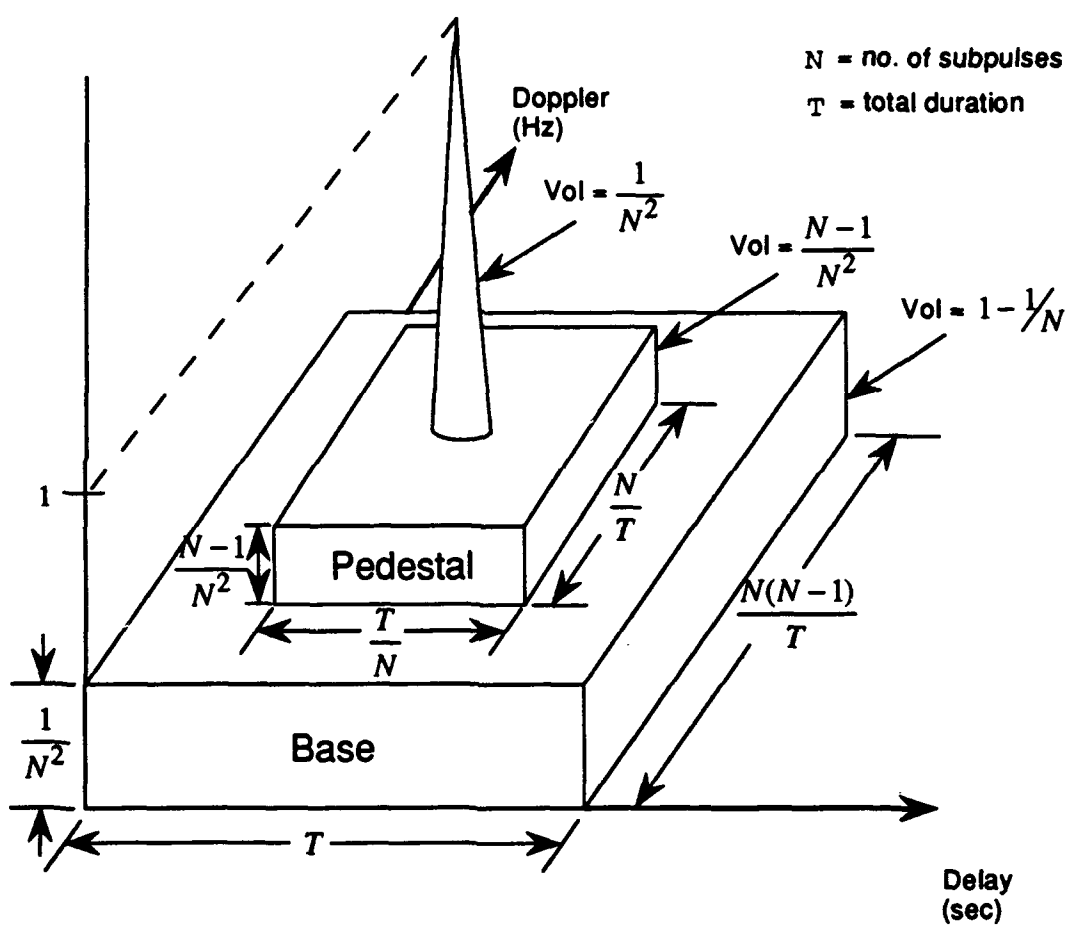


Figure 2.4: Generic Costas Ambiguity Function

It has been shown that when a conventional matched filter is used, the resulting distribution of energy in the delay-Doppler phase plane is the result of the convolution of the ambiguity function and the underlying scattering function. Since volume is conserved in an ambiguity function, when the main lobe is narrow, most of the phase plane energy is the result of the convolution of the pedestal and base portions with the scattering function, which can obscure the main lobe contribution in the presence of dense scattering and additive noise. An example of this phenomenon is shown in Figure 2.5. In this case, the transmit waveform used is a Costas code of Lempel construction with 27 "chips" or subpulses and a time-bandwidth product of 90. The underlying scattering function is comprised of a cluster of eight point scatterers with no additive noise. Even in this case of relatively sparse scattering and no noise, the sidelobe self-clutter significantly obscures the individual point scatterers.

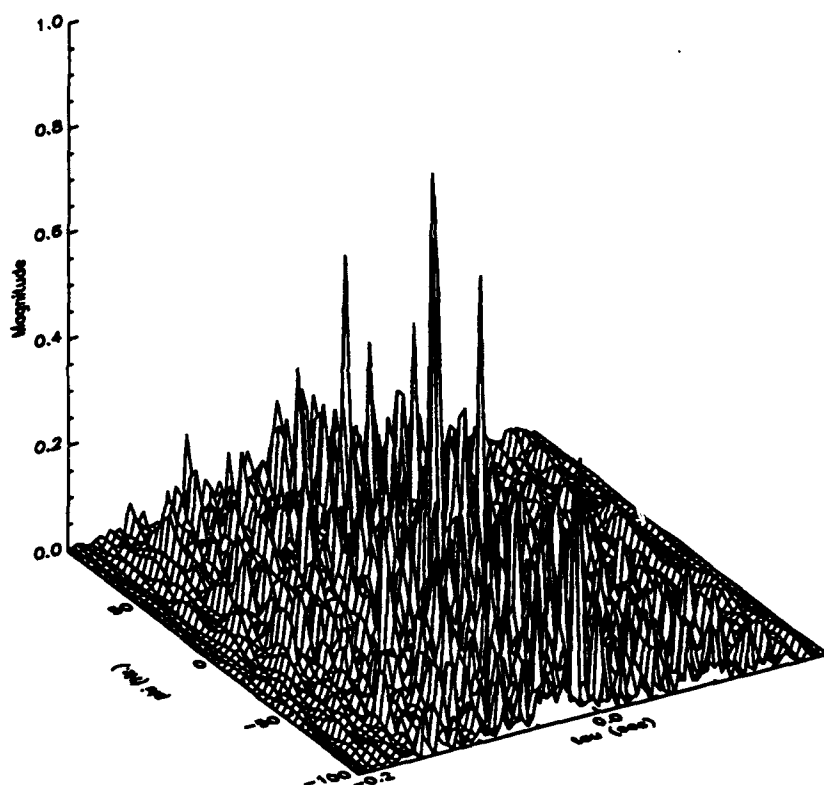


Figure 2.5: Sample Matched Filter Output

Chapter 3

The Uncertainty Product (UP) Receiver

3.1 UP Receiver Structure

Chapter 2 illustrated that the radar uncertainty principle leads to a trade-off between ambiguity mainlobe resolution and sidelobe self-clutter interference in matched filter SF estimation. Mehta and Titlebaum [1, 2] have proposed a new approach for the measurement of scattering functions, which appears to be effective in reducing self-clutter in the phase plane. The basic premise involves passing two signals through the channel and processing each with its own correlation receiver. These outputs are multiplied together to produce a joint statistic l :

$$l = l_f l_g^* / N_0 \quad (3.1)$$

where

$$l_f = \int_{-\infty}^{+\infty} r_f(t) f^*(t - \hat{\tau}) e^{-j2\pi\hat{\phi}t} dt \quad (3.2)$$

and

$$l_g = \int_{-\infty}^{+\infty} r_g(t) g^*(t - \hat{\tau}) e^{-j2\pi\hat{\phi}t} dt. \quad (3.3)$$

The terms $r_f(t)$ and $r_g(t)$ represent the noise corrupted received time series resulting from interrogations by the transmit signals $f(t)$ and $g(t)$ with received energies

E_f and E_g , respectively. The basic structure of the receiver given by (3.1-3.3) is shown in Figure 3.1, where $\hat{\tau}$ and $\hat{\phi}$ represent the hypothesized delay and Doppler coordinates in the phase plane. Generally, the output of the UP receiver will be complex; however, if $f(t) = g(t)$, the receiver reverts to the classic narrowband matched filter which will have a non-negative real output.

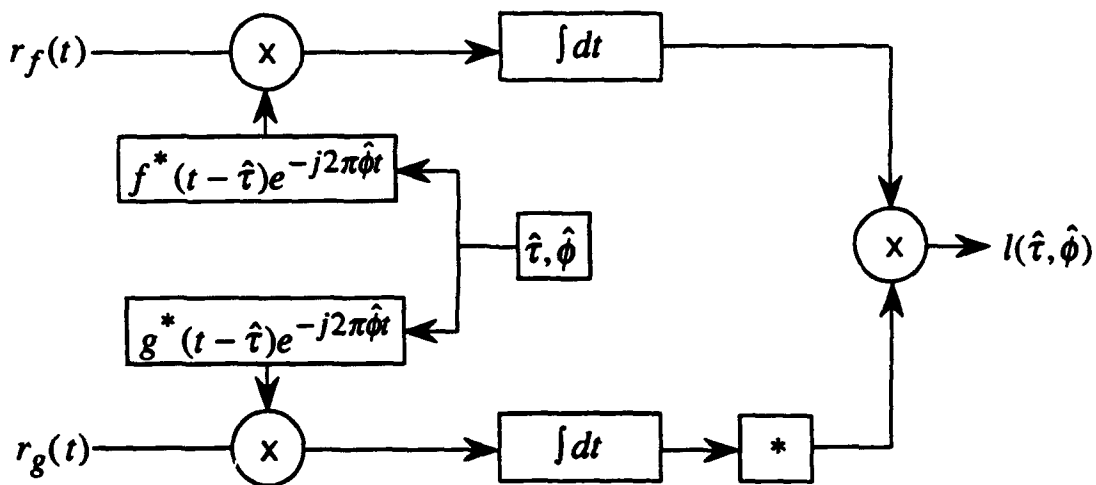


Figure 3.1: The UP Receiver

If the scattering channel is WSSUS, and the noise is uncorrelated between channels, the expected value of the output may be expressed in terms of a scattering function $R_s(\tau, \phi)$ as,

$$\rho_r(\hat{\tau}, \hat{\phi}) = E\{l\}$$

$$= \frac{\sqrt{E_f E_g}}{N_0} \int_{-\infty}^{+\infty} \int_{-\infty}^{+\infty} R_s(\tau, \phi) \Upsilon_{fg}(\Delta\tau, \Delta\phi) d\tau d\phi. \quad (3.4)$$

The term Υ_{fg} in (3.4) is formed by the product of the two signal auto-uncertainty functions

$$\Upsilon_{fg}(\Delta\tau, \Delta\phi) = \chi_{ff}(\Delta\tau, \Delta\phi) \chi_{gg}^*(\Delta\tau, \Delta\phi), \quad (3.5)$$

which we shall refer to as the uncertainty product function (UPF). The auto-uncertainty functions χ_{ff} and χ_{gg} were defined in (2.15), i. e.

$$\chi_{ff}(\Delta\tau, \Delta\phi) = \int_{-\infty}^{+\infty} f(t) f^*(t - \Delta\tau) e^{-j2\pi\Delta\phi t} dt \quad (3.6)$$

and likewise for $g(t)$. Again, we note that if $f(t) = g(t)$, (3.4) reduces to the convolution of the scattering and ambiguity functions given in Equation (2.16), since

$$\Upsilon_{ff}(\Delta\tau, \Delta\phi) = |\chi_{ff}(\Delta\tau, \Delta\phi)|^2 \quad (3.7)$$

Υ_{fg} is not the cross-ambiguity function (CAF) Φ_{fg} which results from transmitting one waveform and processing with another resulting in

$$\chi_{fg}(\Delta\tau, \Delta\phi) = \int_{-\infty}^{+\infty} f(t) g^*(t - \Delta\tau) e^{-j2\pi\Delta\phi t} dt. \quad (3.8)$$

$$\Phi_{fg}(\Delta\tau, \Delta\phi) = |\chi_{fg}(\Delta\tau, \Delta\phi)|^2 \quad (3.9)$$

where χ_{fg} is called the cross-uncertainty function. Generally, a CAF does not

have the auto-ambiguity function structure of a central main lobe surrounded by a lower sidelobe region, but may be considered to consist completely of sidelobes in the sense that its surface may be distributed throughout the phase plane [10]. A simple illustration of this property is shown in Figure 3.2, which is the CAF between an up chirp and a down chirp. Cross-ambiguity functions do, however, possess the volume conservation property of auto-ambiguity functions [11] where

$$\begin{aligned}
 V_\Phi &= \int_{-\infty}^{+\infty} \int_{-\infty}^{+\infty} \Phi(\Delta\tau, \Delta\phi) d\Delta\tau d\Delta\phi \\
 &= E_f E_g.
 \end{aligned} \tag{3.10}$$

The UPF on the other hand, has support only where the supports of the constituent uncertainty functions coincide; thus, for example, the combination of up and down chirp waveforms will result in UPF support only at the origin, as illustrated in Figure 3.3. Clearly, a UPF such as the one in Figure 3.3 can possess the "delta-like" structure which was desired for the ambiguity function of the matched filter receiver. This property is also desirable for the UP receiver due to its similar convolution property. However, because (3.4) is an expected value, it is necessary to study the UPF in greater detail to describe the output of the receiver for a single interrogation and to determine the rate of convergence to its expected value.

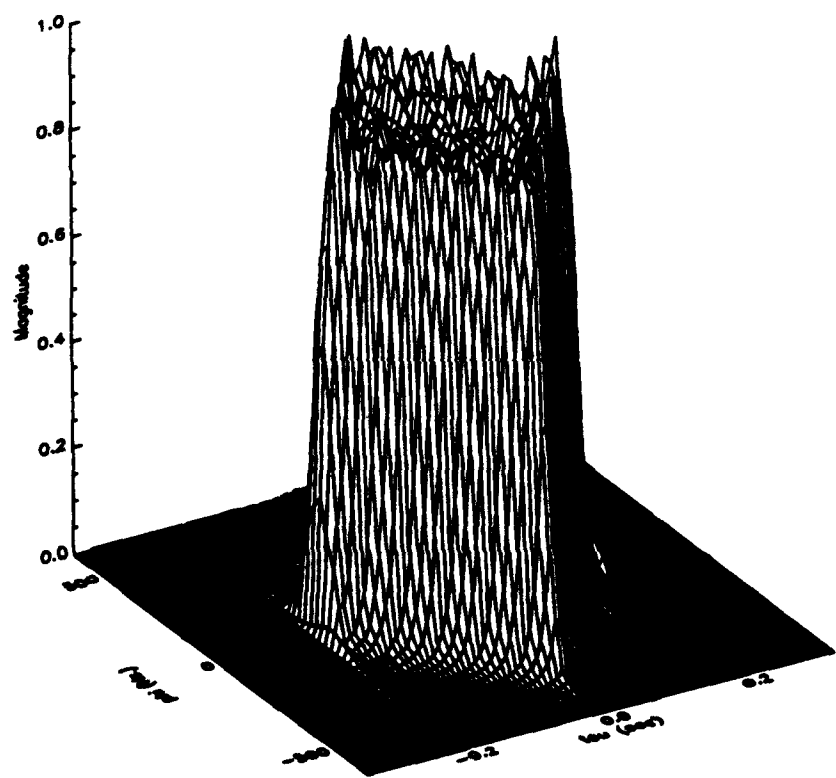


Figure 3.2: Sample Cross-Ambiguity Function

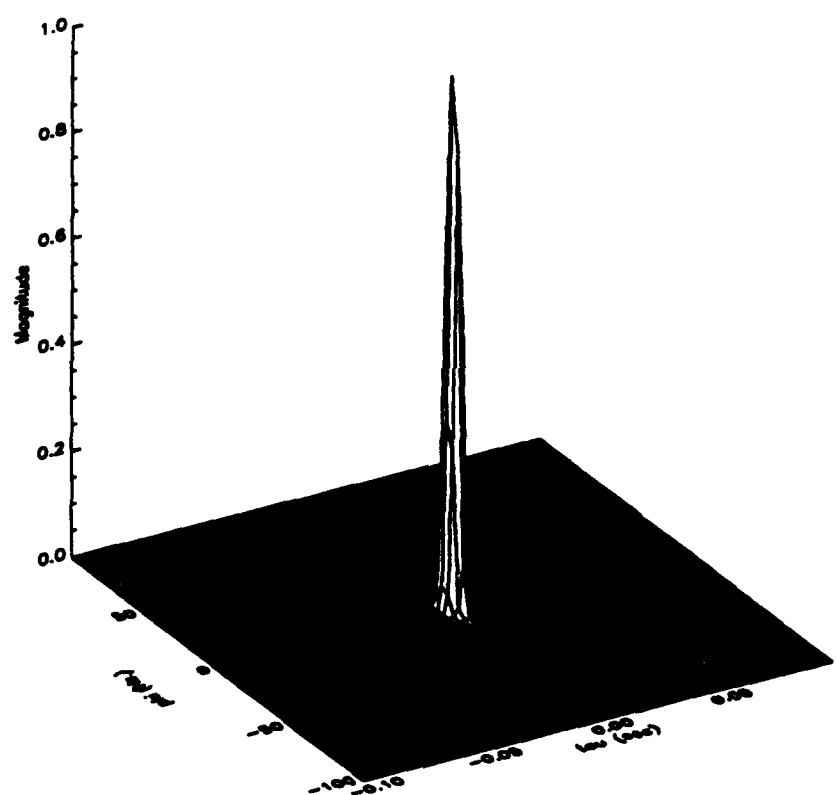


Figure 3.3: Sample Uncertainty Product Function

3.2 UPF Properties

Several basic properties of the uncertainty product function will be derived and contrasted with those of the ambiguity function presented in Chapter 2. In subsequent chapters, these properties will be used to describe UP receiver performance and to compare the rate of convergence to that of the matched filter.

3.2.1 Relationship to the Cross-Ambiguity Function

Titlebaum [15] has extended the self transform property of ambiguity functions to relate the cross-ambiguity functions of four signals, $x_1(t), x_2(t), x_3(t), x_4(t)$, as

$$\int_{-\infty}^{+\infty} \int_{-\infty}^{+\infty} \chi_{x_1 x_2}(\tau, \phi) \chi_{x_3 x_4}^*(\tau, \phi) e^{j2\pi(\tau f - \phi t)} d\tau d\phi = \chi_{x_1 x_3}(t, f) \chi_{x_2 x_4}^*(t, f). \quad (3.11)$$

If we let $x_1(t) = x_3(t) = f(t)$ and $x_2(t) = x_4(t) = g(t)$, (3.11) may be written as

$$\chi_{ff}(t, f) \chi_{gg}^*(t, f) = \int_{-\infty}^{+\infty} \int_{-\infty}^{+\infty} \chi_{fg}(\tau, \phi) \chi_{fg}^*(\tau, \phi) e^{j2\pi(\phi t - f\tau)} d\tau d\phi. \quad (3.12)$$

Note that the product $\chi_{fg} \chi_{fg}^*$ in the integral is the cross-ambiguity function as defined in (3.9). Thus using (3.5) and (3.12) we see that Υ_{fg} and Φ_{fg} are a Fourier transform pair such that

$$\Upsilon_{fg}(t, f) = \int_{-\infty}^{+\infty} \int_{-\infty}^{+\infty} \Phi_{fg}(\tau, \phi) e^{j2\pi(f\tau - \phi t)} d\tau d\phi \quad (3.13)$$

and

$$\Phi_{fg}(\tau, \phi) = \int_{-\infty}^{+\infty} \int_{-\infty}^{+\infty} \Upsilon_{fg}(t, f) e^{-j2\pi(f\tau - \phi t)} dt df. \quad (3.14)$$

Substituting (3.13) into (3.4), the expected UP output may be written as

$$\rho_r(\hat{\tau}, \hat{\phi}) = \frac{\sqrt{E_f E_g}}{N_0} \int_{-\infty}^{+\infty} \cdots \int_{-\infty}^{+\infty} \left[R_s(\tau, \phi) e^{j2\pi(\phi t - \tau f)} \right] \Phi_{fg}(t, f) e^{j2\pi(\hat{\tau} f - \hat{\phi} t)} d\tau d\phi dt df. \quad (3.15)$$

The bracketed term integrated with respect to τ and ϕ is the the Fourier transform of the scattering function, which is defined as the time-frequency correlation function $R_H(f, t)$ [3] and consequently

$$\rho_r(\hat{\tau}, \hat{\phi}) = \frac{\sqrt{E_f E_g}}{N_0} \int_{-\infty}^{+\infty} \int_{-\infty}^{+\infty} R_H(f, t) \Phi_{fg}(t, f) e^{j2\pi(\hat{\tau} f - \hat{\phi} t)} dt df. \quad (3.16)$$

This implies that compact scattering in (τ, ϕ) translates into broad support in (t, f) so that the highest resolution would be obtained from a signal pair with a broad and relatively flat cross-ambiguity profile. The combination of up and down chirp waveforms mentioned earlier is an example of such a pair.

3.2.2 UPF Volume

As mentioned previously, the UPF only has support in the phase plane where the support regions of the constituent uncertainty functions coincide. As illustrated in the up/down chirp example, this implies that, unlike the ambiguity function, the UPF does not conserve volume. In fact, the UPF volume may be

computed by substituting (3.6) into (3.5) and integrating over $(\Delta\tau, \Delta\phi)$ resulting in

$$\begin{aligned} V_T &= \int_{-\infty}^{+\infty} \int_{-\infty}^{+\infty} \Upsilon(\Delta\tau, \Delta\phi) d\Delta\tau d\Delta\phi \\ &= \left| \int_{-\infty}^{+\infty} f(t)g^*(t) dt \right|^2. \end{aligned} \quad (3.17)$$

Clearly, volume is not conserved and in fact may be zero for orthogonal signals.

3.2.3 Maximum Value

Using (3.13) and (3.10) a consequence of the Fourier relationship between the UPF, Υ_{fg} , and the CAF, Φ_{fg} , is that

$$\begin{aligned} \Upsilon_{fg}(0, 0) &= V_\Phi \\ &= E_f E_g \end{aligned} \quad (3.18)$$

and conversely, using (3.14) and (3.17)

$$\Phi_{fg}(0, 0) = V_T. \quad (3.19)$$

Since the volume of the CAF is a positive quantity (Eq. (3.10)), the peak of the UPF at the origin will be a real constant, which depends upon the signal energies. However, unlike ambiguity functions, the UPF sidelobes are in general, complex. The combination of these two facts is the key to the convergence of the UP receiver,

which is shown in Chapter 4.

Chapter 4

Implementation Issues

The convolution of Equation (3.4) and the delta-like uncertainty product function of Figure 3.3 suggest that the UP receiver is capable of producing accurate estimates of scattering structures without the self-clutter often present in the matched filter receiver. However, these results may only be reached in expectation over many realizations. Also, the performance of the UP receiver will be affected by interaction between the two transmit waveforms. Several issues critical to the proper implementation of the UP receiver are discussed below.

4.1 Disjoint Waveform Support

The UP concept requires that the echos from the two constituent waveforms $f(t)$ and $g(t)$ be realizations from the same scattering process. This implies that the waveforms must be transmitted simultaneously or in very close temporal proximity so that the echo $r(t)$ is the result of interrogation by the sum of the constituent waveforms, $x(t) = f(t) + g(t)$, such that

$$r(t) = \sqrt{E_0} \int_{-\infty}^{+\infty} x(t - \tau) S(\tau, \phi) e^{j2\pi\phi\tau} dt + n(t) \quad (4.1)$$

where E_0 is the combined energy of the composite signal, $S(\tau, \phi)$ represents the spreading function of the scattering process, as defined in (2.4), and $n(t)$ is additive noise.

The UP receiver structure shown in Figure 3.1 and given by Equations (3.1-3.3) assumes that the return signal has been separated, by filtering or other means, into two waveforms, $r_f(t)$ and $r_g(t)$, which represent the response of the channel to the transmit waveforms $f(t)$ and $g(t)$, respectively. This separation may not be obtainable; therefore, it is useful to study the test statistics l_f and l_g formed using (3.2,3.3), but with the total echo $r(t)$.

Under the WSSUS assumption, the auto-correlation of the time series (4.1) may be expressed in terms of the scattering function as

$$E\{r(t)r^*(u)\} = E_0 \int_{-\infty}^{+\infty} \int_{-\infty}^{+\infty} x(t-\tau)x^*(u-\tau)R_s(\tau, \phi)e^{j2\pi\phi(t-u)}d\tau d\phi + N_0\delta(t-u) \quad (4.2)$$

where $R_s(\tau, \phi)$ is the scattering function as defined in (2.10) and the noise is assumed to be white. The statistic l given by (3.1), assuming $r(t)$, may be formed as indicated in Figure 3.1 and the expectation $\rho_r(\hat{\tau}, \hat{\phi})$ may be written using (3.1-3.3, 4.2) with $r_f(t) = r_g(t) = r(t)$ as

$$\begin{aligned} \rho_r(\hat{\tau}, \hat{\phi}) = & \frac{E_0}{N_0} \int_{-\infty}^{+\infty} \int_{-\infty}^{+\infty} R_s(\tau, \phi) \left[\int_{-\infty}^{+\infty} x(t-\tau)f^*(t-\hat{\tau})e^{-j2\pi\Delta\phi t}dt \right] \\\left[\int_{-\infty}^{+\infty} x^*(u-\tau)g(u-\hat{\tau})e^{j2\pi\Delta\phi u}du \right] d\tau d\phi \end{aligned}$$

$$\begin{aligned}
&= \frac{E_0}{N_0} \int_{-\infty}^{+\infty} \int_{-\infty}^{+\infty} R_s(\tau, \phi) [\chi_{ff}(\Delta\tau, \Delta\phi) + \chi_{gf}(\Delta\tau, \Delta\phi)] \\
&\quad [\chi_{fg}(\Delta\tau, \Delta\phi) + \chi_{gg}(\Delta\tau, \Delta\phi)]^* d\tau d\phi. \tag{4.3}
\end{aligned}$$

Clearly, this may be expressed in terms of the UPF and cross terms involving auto- and cross-uncertainty functions where

$$\begin{aligned}
\rho_r(\hat{\tau}, \hat{\phi}) &= \frac{E_0}{N_0} \int_{-\infty}^{+\infty} \int_{-\infty}^{+\infty} R_s(\tau, \phi) \Upsilon_{fg}(\Delta\tau, \Delta\phi) d\tau d\phi \\
&+ \left[\frac{E_0}{N_0} \int_{-\infty}^{+\infty} \int_{-\infty}^{+\infty} R_s(\tau, \phi) \{ \chi_{ff}(\Delta\tau, \Delta\phi) \chi_{fg}^*(\Delta\tau, \Delta\phi) \right. \\
&+ \chi_{gf}(\Delta\tau, \Delta\phi) \chi_{gg}^*(\Delta\tau, \Delta\phi) \\
&+ \left. \chi_{gf}(\Delta\tau, \Delta\phi) \chi_{fg}^*(\Delta\tau, \Delta\phi) \} d\tau d\phi \right]. \tag{4.4}
\end{aligned}$$

Cross- ambiguity and uncertainty functions have τ, ϕ plane support equivalent to the support of the convolution of their constituent time-frequency patterns [1, 18]. Consequently, the cross-uncertainty functions χ_{fg} and χ_{gf} have the potential to produce severe self-clutter interference. To minimize these effects, the cross-uncertainty functions of the constituent codes should be negligible in comparison to the uncertainty product in a neighborhood of the origin commensurate in size with the support of the underlying scattering function. As the constituent waveform code orders increase, and the codes become more dense, the cross-ambiguity surface becomes a "mesa" as was shown for the combination of up and down chirps in Figure 3.2. If the waveforms are transmitted simultaneously with the same frequency support, the cross-ambiguity surface will be centered at the origin which would maximize the

undesirable cross-uncertainty effect. A solution to this problem is to use disjoint waveforms which occupy different areas of the time-frequency plane.

Consider two waveforms $f(t)$ and $g(t)$ which occupy bounded, but disjoint, areas in the time-frequency plane as illustrated in Figure 4.1. The support regions for $f(t)$ and $g(t)$ do not overlap and are separated by a time-frequency interval such that a cross-ambiguity clear area of dimension $\Delta\tau_c, \Delta\phi_c$ will be formed about the origin. If this clear area is made larger than the support of the underlying scattering distribution, there will be no cross-ambiguity effects. Generally, some prior information concerning the support of the scattering function will be necessary in order to center the clear area in the time-frequency plane. For example, if the scattering support is known to have range extent L , the echos corresponding to the signals $f(t)$ and $g(t)$ will be distinct if

$$\Delta\tau_c \geq 2L/c. \quad (4.5)$$

Likewise, the echos will be spectrally distinct if

$$\Delta\phi_c \geq (2\phi_s + .5(B_f + B_g)) \quad (4.6)$$

where ϕ_s is the scattering Doppler support and B_f and B_g are the signal bandwidths. A candidate waveform pair may be generated by separating a V-chirp waveform into disjoint up and down chirps as shown in Figure 4.2. The cross-ambiguity functions generated from this pair will have no support at the origin

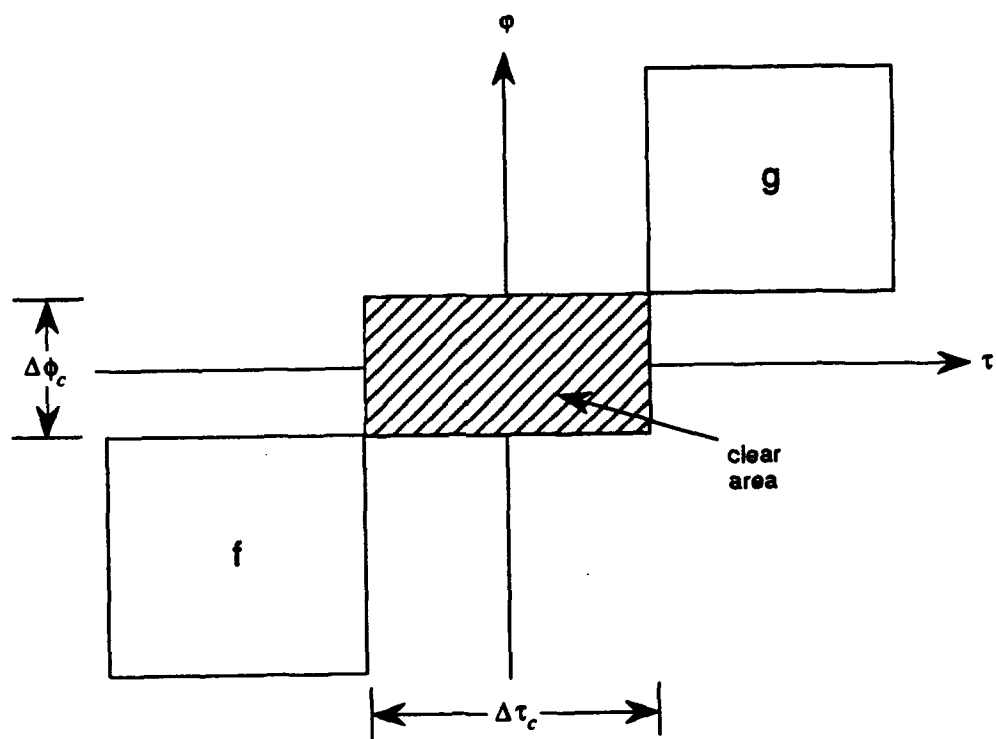


Figure 4.1: Disjoint Waveform Support

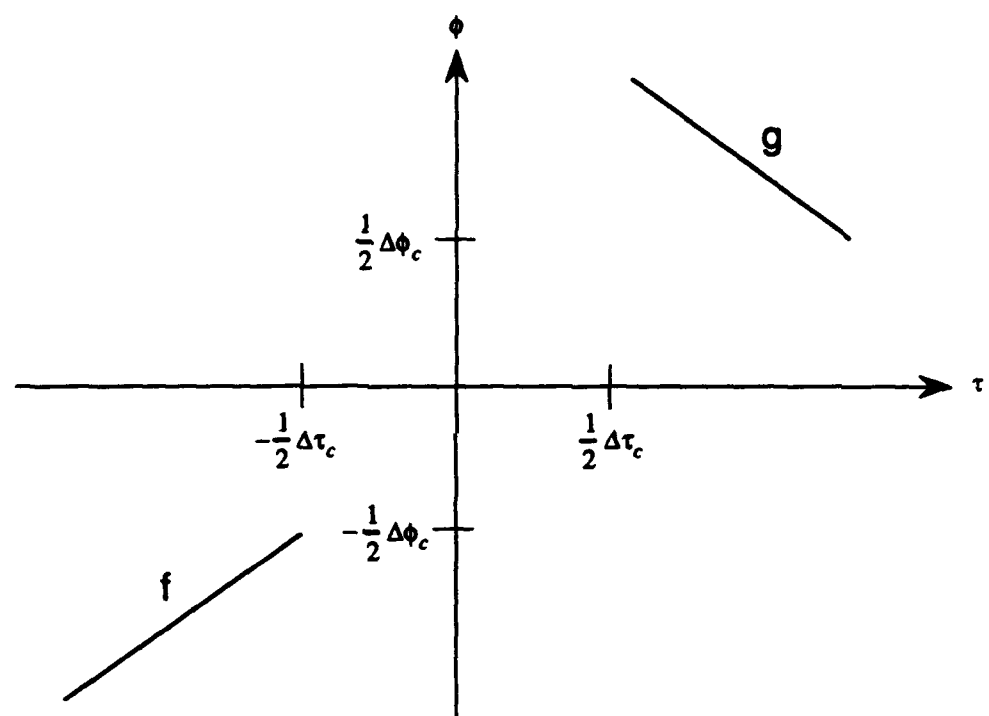


Figure 4.2: The Disjoint V-chirp Waveform

and will consist of two diamond shaped mesas (one in each branch of the receiver) centered at

$$(\Delta\tau, \Delta\phi) = \pm(\Delta\tau_c/2 + T, \Delta\phi_c + B) \quad (4.7)$$

each of height $1/2BT$ where B and T are the bandwidth and duration of the individual chirps [10]. A plot of the output from the lower branch of the receiver, l_f , is shown in Figure 4.3. Note that the correlation of the replica for the lower branch, $f(t)$, with the composite waveform, $x(t)$, produces two regions of support in the range-Doppler plane. The surface centered at the origin is the auto-ambiguity function for $f(t)$ while the diamond-shaped mesa in the upper-right quadrant is the cross-ambiguity function of the two waveforms. A similar output is obtained for the upper branch of the receiver, l_g , with the auto-ambiguity function of the down chirp, $g(t)$, centered at the origin and a cross-ambiguity mesa in the lower-left quadrant. Recall that the uncertainty product function only has volume where both branches of the receiver have support. Thus, in addition to being outside the clear area, the cross-ambiguity effects from each branch will be suppressed by the lack of volume in the same region of the opposing branch, placing the majority of UPF volume at the origin where the up and down chirp auto-ambiguity functions coincide. Effects of the suppressed cross-ambiguity contributions will only become noticeable when the clear area is not large enough to encompass the scattering process and when dense scattering causes many suppressed CAF contributions to overlap. With this in mind, it should also be noted that it is desirable to keep the clear area as small as possible since the basic assumptions underlying UP processing are that the WSSUS

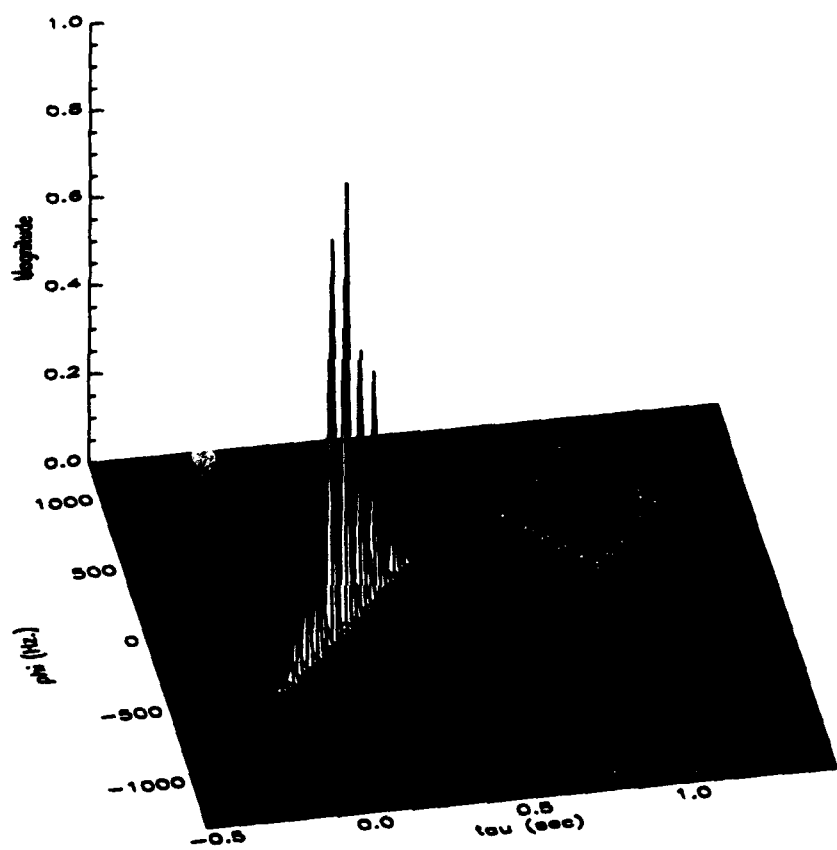


Figure 4.3: Disjoint V-chirp Output for l_g

conditions hold and that the scattering process realization interrogated by each of the signals is the same.

4.2 Simultaneous Observability

If the signals are disjoint, as indicated in Figures (4.1, 4.2), it is necessary that the scattering process be observable by both branches of the UP processor shown in Figure 3.1 for the same hypothesis $(\hat{\tau}, \hat{\phi})$. In other words, when a scatterer is hypothesized at a position $(\hat{\tau}, \hat{\phi})$ by the first signal transmitted, $f(t)$, the mainlobe of the uncertainty function of the second, $g(t)$, must have sufficient range delay support (τ_g) so that the scatterer is observable or,

$$\frac{2|v|T_d}{c} \leq \tau_g \quad (4.8)$$

where

$$T_d = (\Delta\tau_c + .5(T_f + T_g)) \quad (4.9)$$

is the effective delay between the signals, T_f, T_g are the signal durations, and v is the scatterer Doppler velocity.

Since v is estimated by the Doppler hypothesis $\hat{\phi}$ via

$$\frac{2v}{c} = \frac{\hat{\phi}}{f_0} \quad (4.10)$$

where f_0 is the frequency centroid, the bound for τ_g may be expressed as

$$\frac{\hat{\phi}T_d}{f_0} \leq \tau_g. \quad (4.11)$$

Moreover, the range delay resolution of a waveform with envelope bandwidth B_g is

$$\tau_g = k/B_g \quad (4.12)$$

where k is a constant which depends upon the chosen definition of resolution (e. g. 3 dB down). Consequently, (4.6) may be formulated as a bound on scatterer Doppler

$$\hat{\phi} \leq \frac{kf_0}{B_g T_d} \quad (4.13)$$

which must not be exceeded unless the delay hypothesis of the second signal is Doppler compensated. An approach suggested in [1] when a high resolution Costas type waveform is used for the first signal, is to use a CW for the second signal $g(t)$ which has range resolution equivalent to its duration.

A more elegant solution which avoids the need to bound $\hat{\phi}$ and allows for the use of high resolution codes for both $f(t)$ and $g(t)$, is to compensate the delay hypothesis of the second signal based upon the overall Doppler hypothesis. Consider a particular phase plane cell corresponding to the hypothesis $(\hat{\tau}, \hat{\phi})$. The upper branch of the processor shown in Figure 3.1, which is a matched filter for the first signal $f(t)$, uses the parameters $(\hat{\tau}, \hat{\phi})$ to form the filter. Assuming that the

time base origin for both signals coincides with the transmit leading edge of $f(t)$, the lower branch, which corresponds to the second or lagging signal $g(t)$, must use a delay hypothesis $\hat{\tau}_g = \hat{\tau} + T_d$ in order to bring it into coincidence with the first signal echo. If however, $\hat{\phi}$ is not zero, the delay between the signals will be dilated by the factor

$$\begin{aligned}\beta &= 1 + 2v/c \\ &= 1 + \hat{\phi}/f_0.\end{aligned}\quad (4.14)$$

Thus, in order to compensate the delay hypothesis $\hat{\tau}_g$, it is necessary to use

$$\hat{\tau}_g = \frac{\hat{\tau} + T_d}{\beta}. \quad (4.15)$$

Analogously, it is also necessary to use a slightly different Doppler hypothesis for the second signal to compensate for Doppler change occurring over the total signal duration. This effect is not directly measurable unless a quadratic (acceleration) parameter is included in the matched filter [16]. This is not done in the structure proposed herein and thus both branches of the UP processor use the same Doppler hypothesis. Spectral dilation due to high Doppler can be compensated by using a wide band matched filter rather than the narrowband version presented here.

In practice, a straightforward solution to the compensation problem exists which avoids the need to bound $\hat{\phi}$ by automatically compensating the delay hypothesis of the second signal based upon the overall Doppler hypothesis. This method

involves a modification to the two replicas for $f(t)$ and $g(t)$ in the two branches of the receiver in Figure 3.1. The transmit waveform and the two UP receiver replicas are shown graphically in Figure 4.4. The first, $x(t)$, is the composite transmit waveform with duration $T_x = T_f + \Delta\tau_c + T_g$, where T_f, T_g , and $\Delta\tau_c$, are the durations of the original waveforms and the clear area, respectively. The second and third waveforms, $f(t)$ and $g(t)$, are the waveforms to be used for replica formation in the two branches of the UP receiver. The difference in the receiver occurs in the specification of the waveform $g(t)$. Note that this signal is defined as having a leading “dead time” of duration $T_f + \Delta\tau_c$. By adjusting the time base of $g(t)$ to account for the delay between the two receiver branches, the replica formation for the hypothesized Dopplers, $\hat{\phi}$, automatically incorporates any time compression caused by the scattering function’s motion.

4.3 Virtual Scattering

It is important to understand that the UP receiver output given by the convolution of Equation (3.4) is an expected value. However, it is instructive to demonstrate the receiver output for one realization of a deterministic scattering process. Consider a scattering function consisting of two scatterers separated by 25 meters, both at zero Doppler, ensonified using the disjoint V-chirp waveform shown in Figure 4.2. The waveforms chosen for this example each have a duration of 200 milliseconds and a bandwidth of 450 Hz. The clear area for this waveform pair is $\Delta\tau_c = 400$ milliseconds in range delay and $\Delta\phi_c = 200$ Hz in Doppler, which

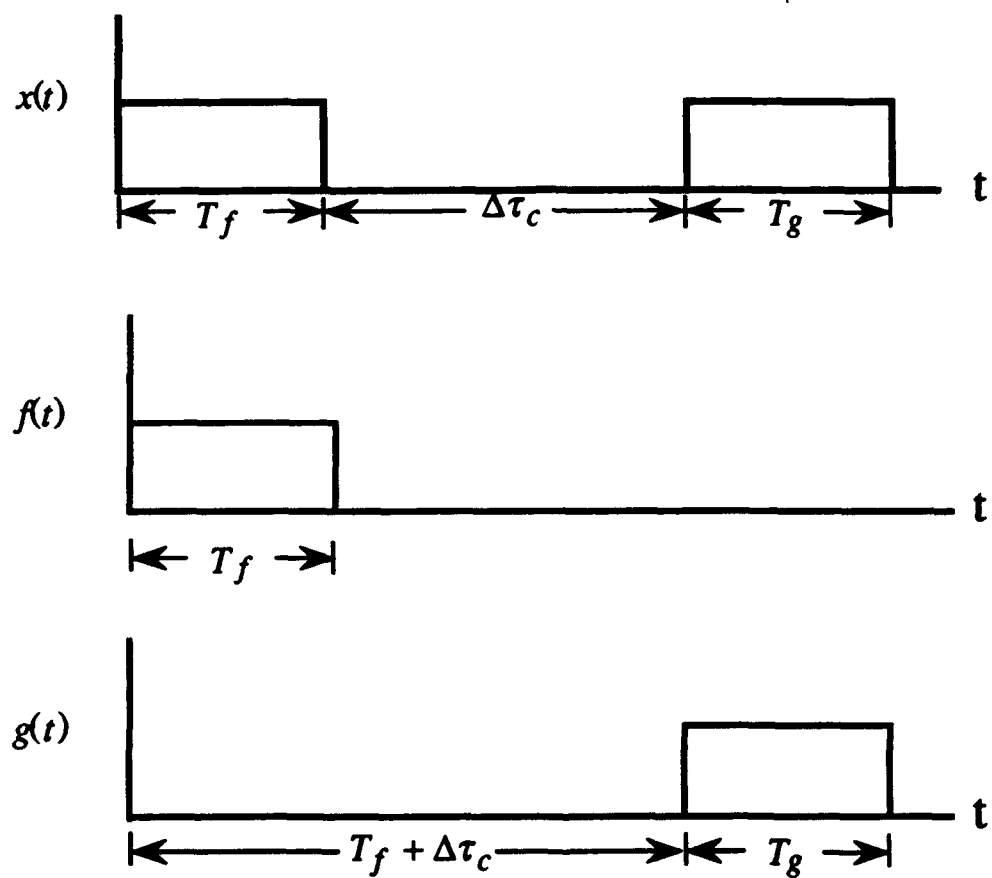


Figure 4.4: UP Receiver Waveforms

is sufficient to provide an unambiguous scatterer image. One realization of the UP receiver is shown as a phase plane plot with axes τ (delay) and ϕ (Doppler shift) in Figure 4.5. The magnitude of the receiver output is displayed so that the energy units of the UP receiver output will agree with those of the matched filter.

Although the UPF of the chirp waveforms does approach a "thumbtack" (see Fig. 3.3) with support only at the origin, one realization does not produce an accurate estimate of the underlying scattering process. The two returns at zero Doppler are from the point scatterers; however, the two returns at non-zero Doppler are caused by the interaction of the two waveforms' auto-uncertainty functions for each scatterer, and may be termed "virtual scatterers." This phenomenon is depicted in Figure 4.6, where the outputs of the two branches of the receiver (l_f, l_g) and their product are displayed.

A scattering process may be described as a continuous or discrete scattering distribution in delay and Doppler. Each point within this distribution can be described in terms of a complex, random, and time-varying impulse response, which in turn can be modeled as a Gaussian process with Rayleigh magnitude and uniform phase [3, 6]. A discrete scattering process $S(\tau, \phi)$ can be modeled as a collection of point scatterers at positions (τ_i, ϕ_i) in the phase plane with complex reflectivity u_i , given by

$$u_i = x_i + jy_i \quad (4.16)$$

where the x_i 's and y_i 's are uncorrelated Gaussian random variables with zero mean and a standard deviation of one. Since the expected value of the receiver output

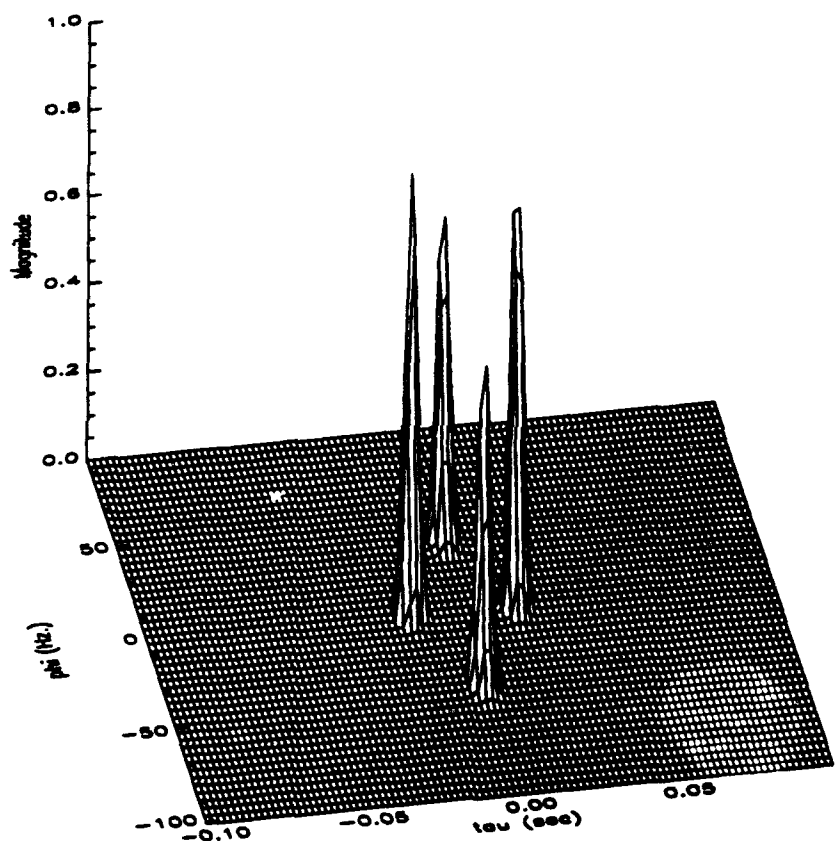


Figure 4.5: UP Receiver Output for a Deterministic Scattering Function

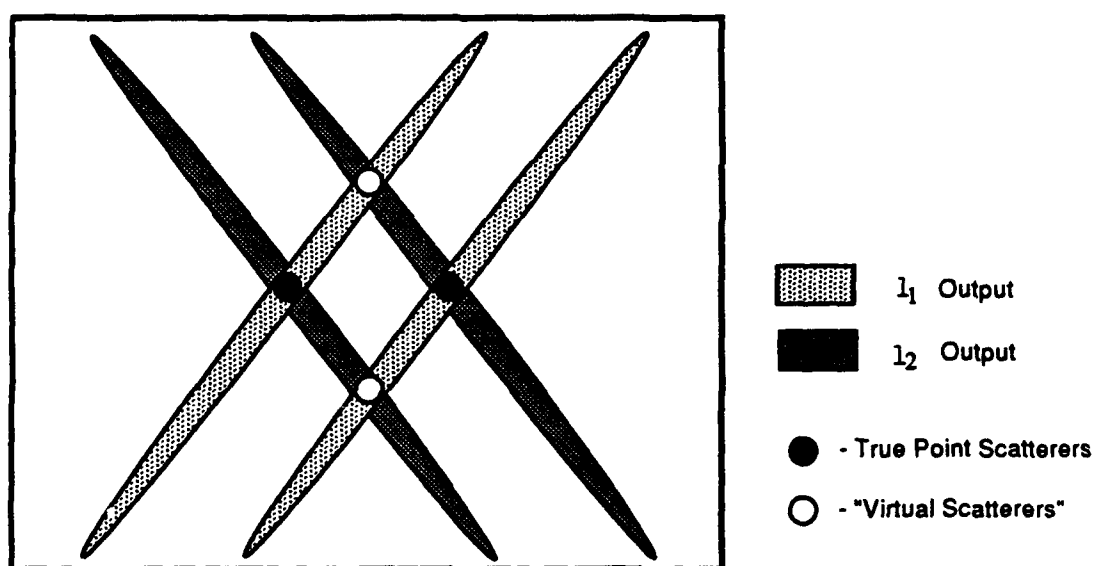


Figure 4.6: Uncertainty Function Interaction

is given by (3.4), the response at (τ, ϕ) corresponding to the true scatterer positions will be real and proportional to $\Upsilon_{fg}(0, 0)$, which from (3.18) is equivalent to the volume of the cross-ambiguity function Φ_{fg} . Also, under WSSUS conditions, scatterers at different points in the phase plane are uncorrelated. Therefore, the “virtual scatterers” that appear at the processor output represent complex random contributions of separate scattering sites, which will tend to cancel out when a number of realizations are averaged.

The expected rate of decay of the sidelobe structure of the UP receiver may be studied by examining the decay of one phase plane bin within a “virtual scatterer.” The ensemble average of any one of these phase plane points may be represented by the sum

$$s_{ij} = K_i K_j \frac{1}{N} \sum_{k=1}^N u_{ik} u_{jk}^* \quad (4.17)$$

where N represents the number of realizations and u_{ik} and u_{jk} represent the reflectivity of the two scatterers for the k^{th} realization. Here, K_i and K_j are constants which scale the scatterers’ reflectivities u_{ik} and u_{jk} by the two uncertainty functions’ magnitude at the given phase plane point. Because these reflectivities are uncorrelated random variables, we may determine the rate of convergence via the Central Limit Theorem [17].

Theorem 4.3.1 Central Limit Theorem: *Let $f(\cdot)$ be a probability density function with mean μ and finite variance σ^2 . Let \bar{X}_N be the sample mean from a random sample of size N from $f(\cdot)$. Let the random variable Z_N be defined by*

$$Z_N = \frac{\bar{X}_N - E[\bar{X}_N]}{\sqrt{\text{var}[\bar{X}_N]}} = \frac{\bar{X}_N - \mu}{\sigma/\sqrt{N}}. \quad (4.18)$$

Then, the distribution of Z_N approaches the standard normal distribution as N approaches infinity.

Equation (4.18) says that the mean from N random samples \bar{X}_N taken from any distribution with mean μ and finite variance σ^2 approaches a normal random variable with mean μ and variance σ^2/N as $N \rightarrow \infty$. Therefore, the average s_{ij} , i. e. the virtual scatterer level, will tend to zero (the mean) as $O(\frac{1}{\sqrt{N}})$.

The disjoint V-chirp waveform and a fluctuating version of the two-point scattering function discussed above will be used to demonstrate the convergence of the UP receiver. Since WSSUS conditions are necessary, we will assume that our reflectivities, u_{ij} , remain fixed for one realization only. The ensemble averaged output of N realizations of the UP receiver is shown in Figures 4.7 (a)-(d) for various values of N . Figure 4.7 (a) displays the magnitude of the output from the first realization showing the two point scatterers and the two “virtual scatterers” expected for this scattering function. In Figures 4.7 (b)-(d) we see that the purely real mainlobes of our true scatterers reinforce each other while the “virtual scatterers” decay as predicted.

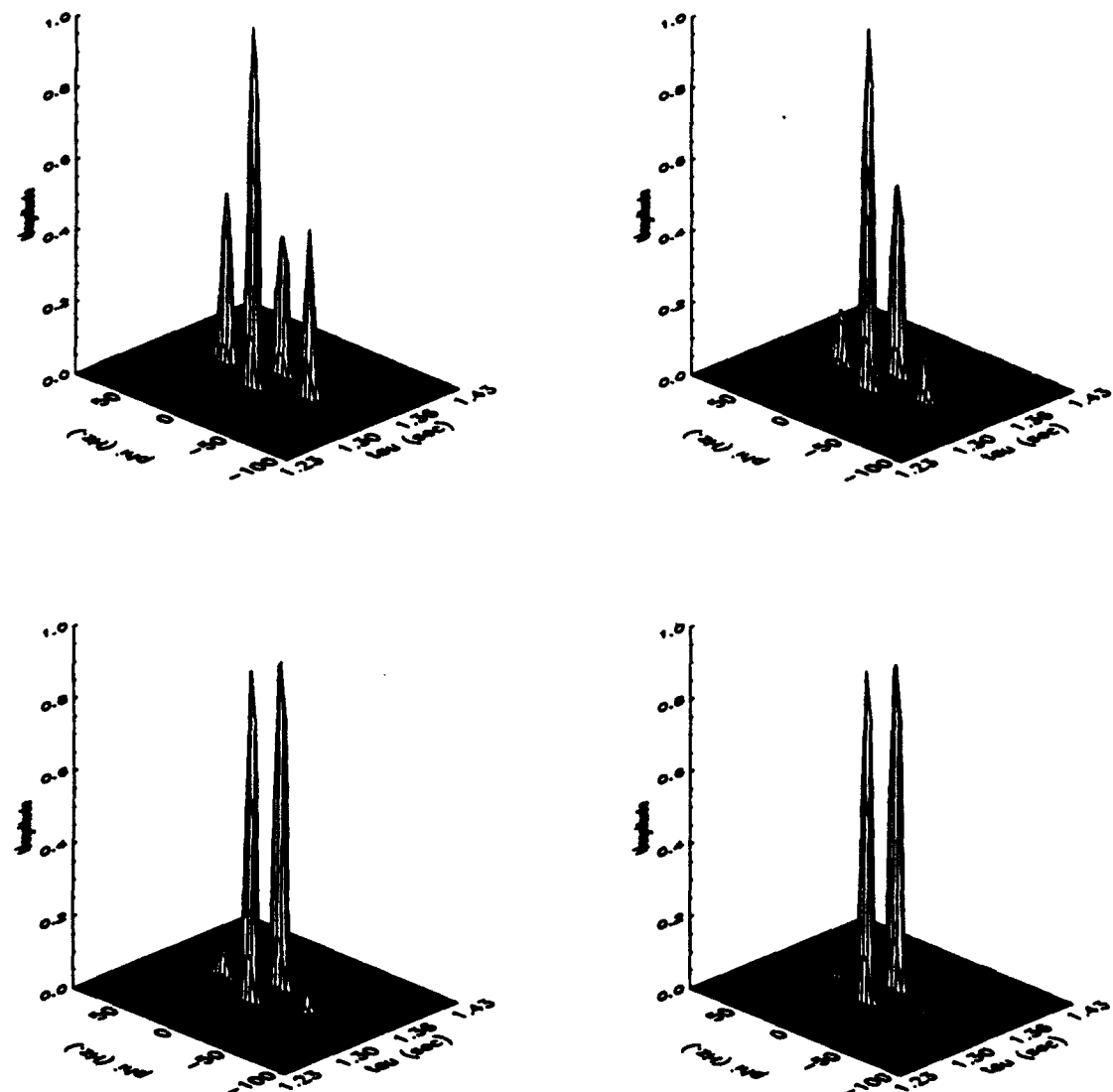


Figure 4.7: UP Receiver Output for N Realizations: (a) $N = 1$, (b) $N = 10$, (c) $N = 100$, (d) $N = 300$

For comparison, the same scattering function as above was interrogated using a Costas coded waveform with a main lobe resolution comparable to that of the UPF for the disjoint V-chirp waveform. Results are shown in Figures 4.8 (a)-(d). Figure 4.9 shows the average background, N_a , for each of the receivers as a function of the number of iterations N . The background level decreases steadily for the UP while the background level of the matched filter is relatively constant, in this noise-free case, due to the sidelobe clutter which is predicted by the ambiguity function's conservation of volume.

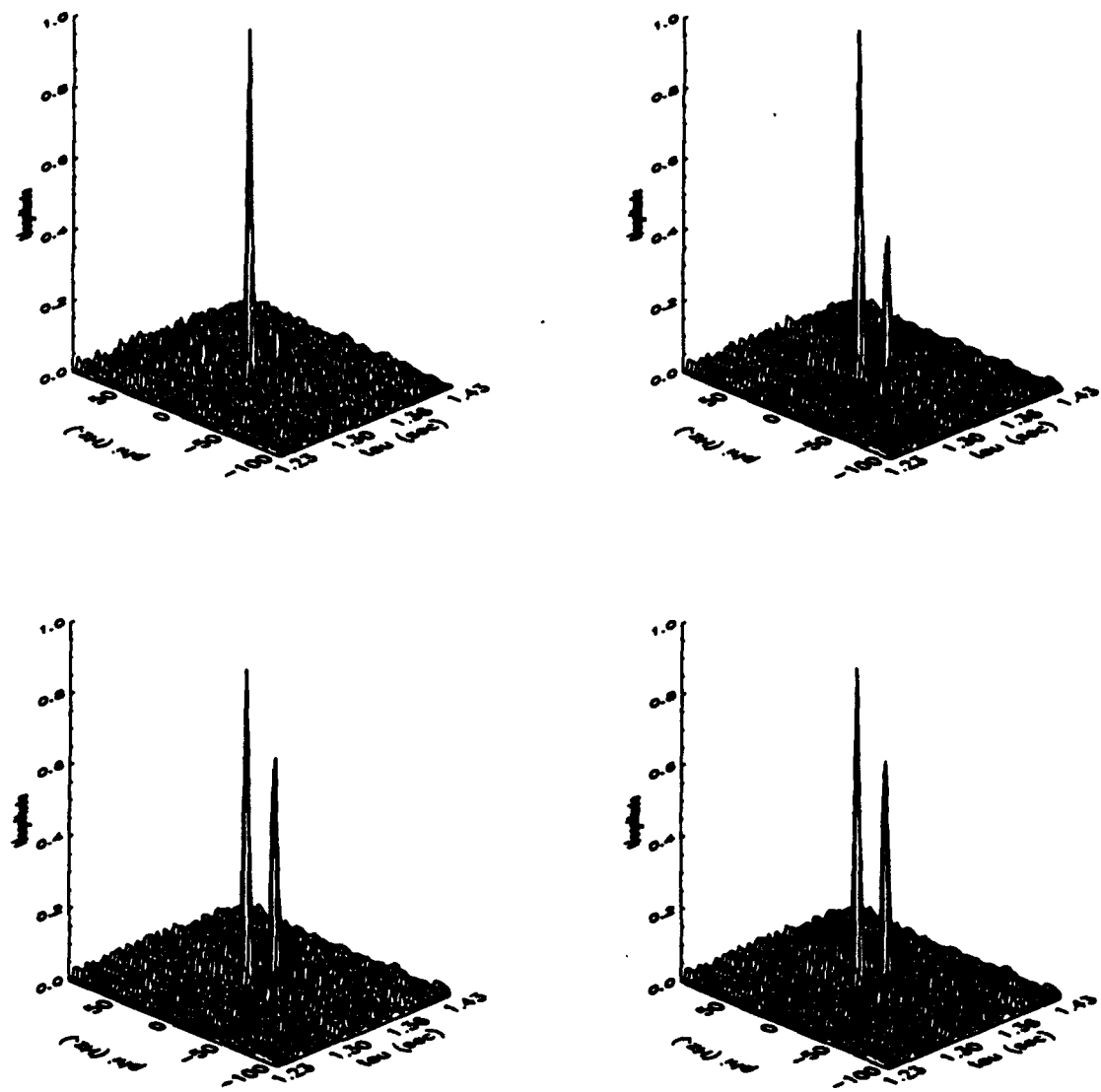


Figure 4.8: Matched Filter Output for N Realizations: (a) $N = 1$, (b) $N = 10$,
(c) $N = 100$, (d) $N = 300$

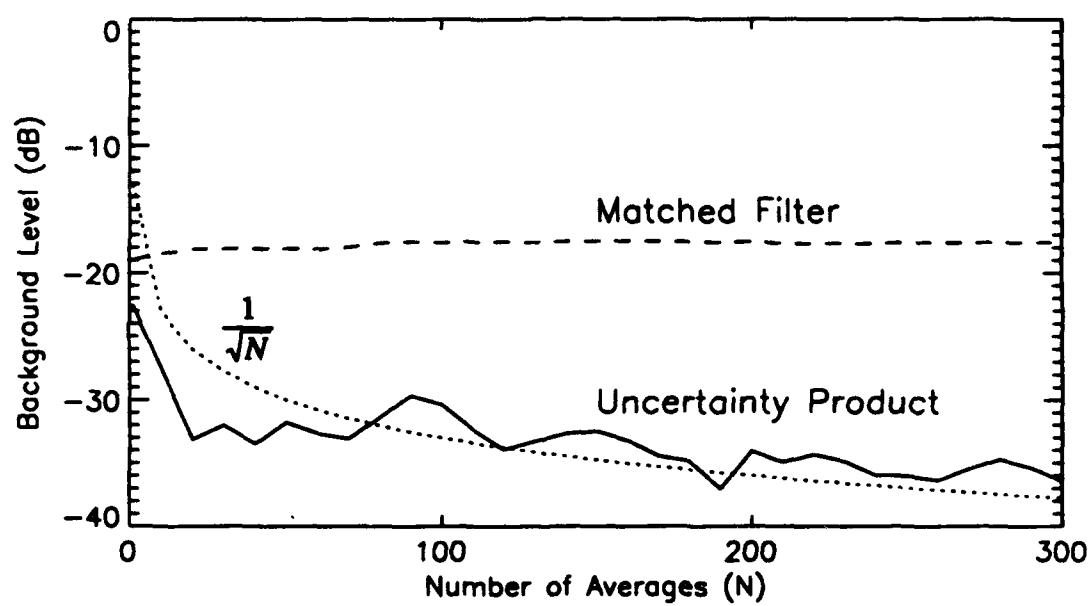


Figure 4.9: Receiver Background Comparison

Chapter 5

Waveform Design Considerations

Thus far, the response of the UP receiver has only been demonstrated for the combination of up and down linear FM (or chirp) waveforms. In fact, many pairs of waveforms may be combined to produce a UPF capable of resolving fine scattering function structure. If such resolution exists and a sufficient clear area may be defined, then the expected output of the receiver will converge to an unambiguous estimate of the scattering process. In Chapter 4 the concept of virtual scattering was introduced to describe the effects that the interaction of the two waveforms' auto-uncertainty functions have on resolution. In some cases, such as the up/down chirp combination, distinct virtual scatterers will be formed with amplitudes commensurate with those of the true point scatterer responses. However, when two frequency hop waveforms are used, the virtual scattering effects can be more subtle and less predictable due to the interaction between the pedestals of the two waveforms. *A priori* information about the basic structure of the scattering process can, in some instances, aid proper waveform selection to reduce the effects of virtual scattering on a single interrogation, and thus improve receiver performance. Therefore, it is useful to review basic waveform constructions and their associated auto-ambiguity functions in order to predict the UPF characteristics of any given pair.

In the following sections various waveform constructions will be presented along with sample auto-ambiguity functions. Also, the hit array [7] will be introduced as a tool to describe auto- and cross-ambiguity sidelobe structure for hop-coded waveforms, and the product of hit arrays [18] will be used to predict UPF composition. Code density, i.e., the number of chips for a given signal duration and bandwidth, will be discussed in terms of the validity of hit array use and the differing UPF implications between sparse and dense hop codes. Finally, waveform pair selection will be discussed in particular cases where some degree of information about the scattering function is known.

5.1 Component Waveforms

For many years waveforms have been designed for use in radar and sonar applications. Although some of the traditionally used waveforms, such as CWs or linear FMs, are not capable of simultaneous resolution in both time and frequency, the UPF of two such waveforms may be. In addition, time-frequency hopped (hop-coded) waveforms, which often achieve simultaneous range and Doppler resolution, can benefit from reduced sidelobes when used in the UP receiver.

5.1.1 The CW

The CW, which is the simplest of waveforms commonly used in matched filter processing, is given by

$$x(t) = A(t)e^{-j2\pi f_{ct}t}, 0 \leq t \leq T \quad (5.1)$$

where f_o is the transmit center frequency and T is the total signal duration. In addition, the term $A(t)$ represents the amplitude shading or "window" applied over the duration of the pulse. Amplitude shading of the pulse with any of the commonly used windows (Taylor, Hamming, Hanning, etc.) will result in more rapidly decaying ambiguity sidelobes than when a unit amplitude window is used [19]. Figure 5.1 is an illustration of this process. In the figure, the auto-ambiguity function is displayed for a CW of the same duration as the CW in Figure 2.3, where a Hamming window has now been applied to the pulse. The quickly decaying sidelobes evident in the figure are desirable when a CW is used as a UP waveform since the amount of energy coincident with the opposing branch of the receiver is lessened for both the UPF and the CAF contributions. As previously mentioned, a CW pulse has a time-bandwidth product $TW = 1$ implying a symmetric ambiguity mainlobe with high resolution possible in either range or Doppler, but not both.

5.1.2 The Linear FM

The linear frequency modulated (LFM), another waveform traditionally used in matched filter processing, is defined by the function

$$x(t) = A(t)e^{-j2\pi(f_o t + \frac{W}{2T}t^2)}, 0 \leq t \leq T \quad (5.2)$$

where $A(t)$, f_o , and T are defined above and W is the signal frequency excursion. An example of a LFM signal with $T = 0.2$ seconds and $W = 450$ Hertz is shown in Figure 5.2. In this case, a unit amplitude (rectangular) window was used for

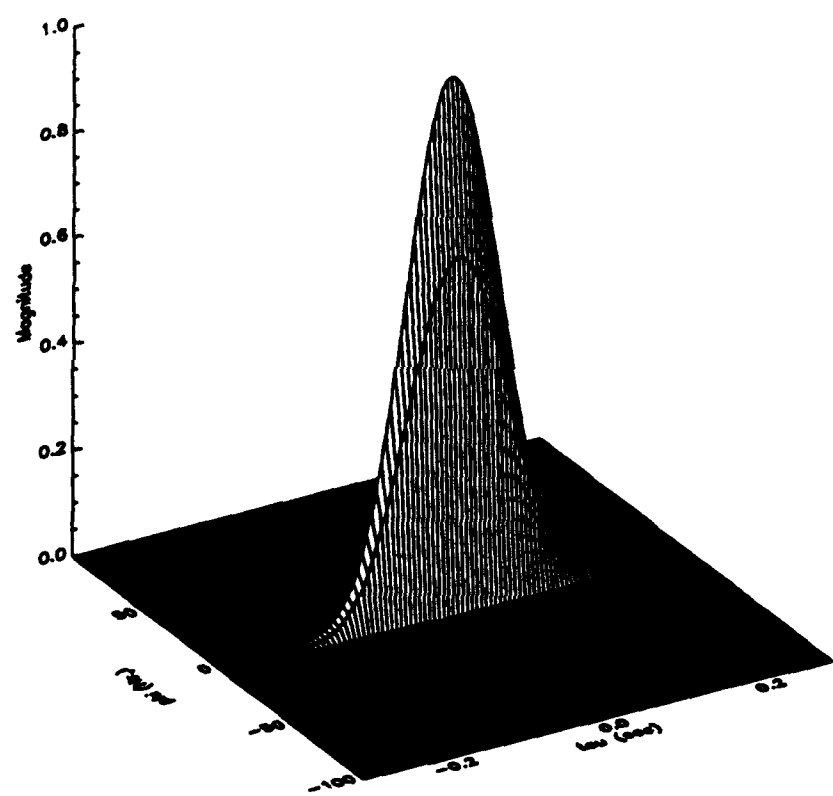


Figure 5.1: Hamming Windowed CW Pulse

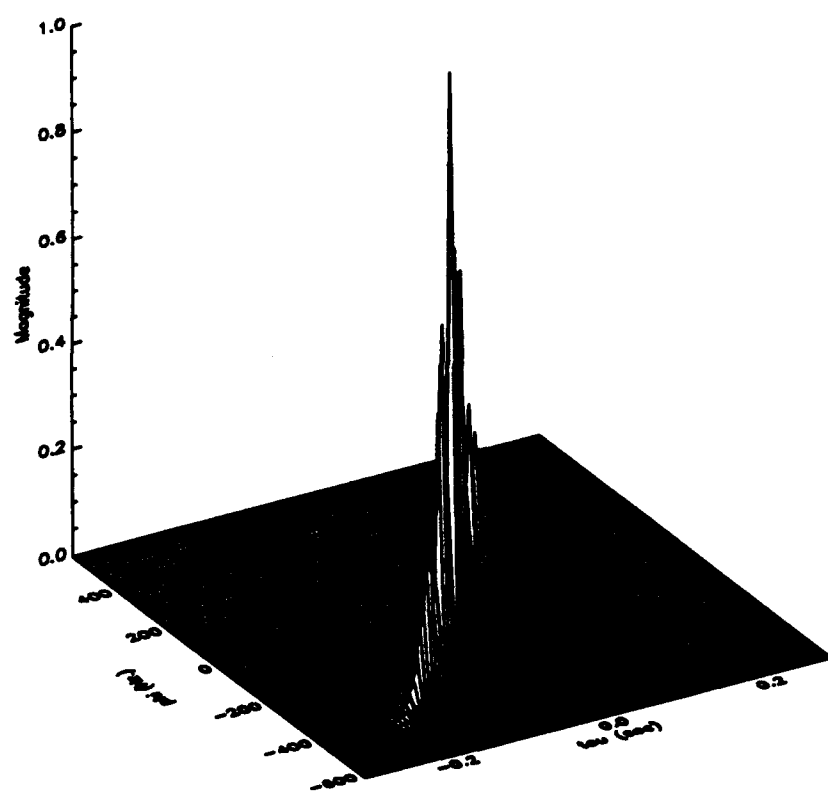


Figure 5.2: Sample Linear FM

the duration of the pulse, as is often the case when using LFM waveforms. Note that with the LFM there is a strong coupling between range resolution and Doppler resolution. For this reason, the LFM by itself is generally not useful for scattering function identification.

Although LFM waveforms are often used without amplitude shading, proper windowing can provide a significant reduction in UPF and CAF effects when using such waveforms in the UP receiver. In Figure 3.3 the UPF for an up and down chirp combination was shown where Hamming windows were applied to the LFMs. This windowing had the effect of suppressing both the cross-ambiguity effects and the contribution of the coincident auto-ambiguity effects within the clear area. As a counter example, consider the UPF for the same two waveforms where unit amplitude windows are used, as shown in Figure 5.3. In the presence of multiple scatterers, the two sidelobe "arms" present in this UPF will tend to produce stronger virtual scatterers and more self-clutter once the receiver converges to its expected value.

5.1.3 Frequency Hop-Coded Waveforms

In recent years, a significant amount of signal design work has been directed toward the study of time-frequency hopped (hop code) signals in attempts obtain waveforms which are highly resolvent in both range and Doppler with relatively flat sidelobe pedestals [12, 14, 20, 21, 22]. The general form of a hop-coded waveform

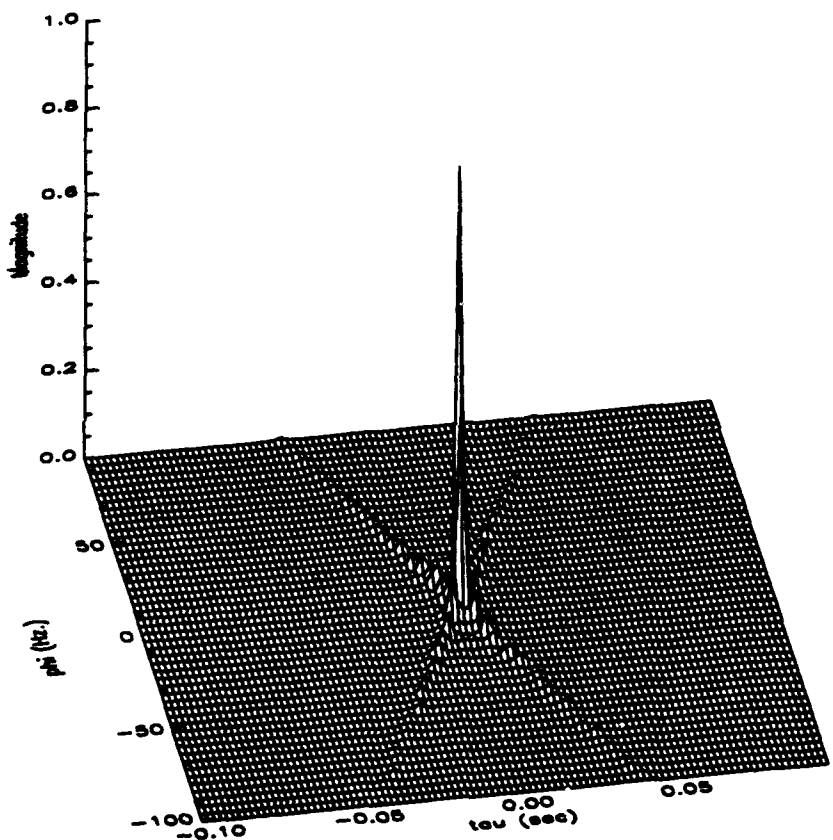


Figure 5.3: Disjoint V-chirp UPF with Rectangular Window

of N subpulses is given by

$$x(t) = \sum_{k=1}^N A_i(t) e^{j2\pi[(f_0 + f_k)t + \phi_i]}, \quad (5.3)$$

where f_0 is the center frequency, f_k is the frequency offset of the k -th pulse or "chip" from the center frequency, and ϕ_i is a constant phase shift that is introduced to assure continuity of the waveform at pulse-to-pulse transitions in the time domain. The waveform description given by Equation (5.3) can be used to describe a wide variety of waveforms in discrete terms. For example, the CW pulse given by Equation (5.1) can be formulated discretely with a code of order $N = 1$ with $f_1 = 0$.

Discrete waveforms may be designed with chips of unequal length and frequency spacing. Often this formulation is used to approximate a continuous waveform such as an exponential or parabolic frequency allocated code. For this discussion we shall assume that the frequency modulation f_k operates on an equi-spaced grid where each cell is of size T_s seconds in duration and the distance between adjacent cell centers in frequency is Δf Hertz. Figure 5.4 shows a simple time-frequency pattern on such a grid for a code with five subpulses. Note that for each time index, k , there is a unique frequency slot, $I(k)$. Waveform codes which exhibit this property are referred to as *full codes*. Codes where all of the time and frequency slots are not used are termed *non-full codes*. If the desired subpulse duration, T_s , and subpulse frequency spacing, Δf , of a code are known, then the time-frequency

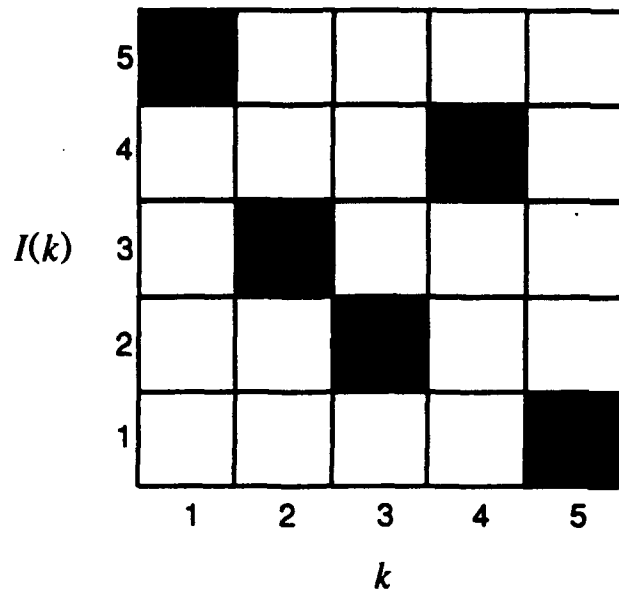


Figure 5.4: Sample Time-Frequency Pattern

pattern of the waveform can be described completely by a discrete function $I(k)$ for $k = 1, \dots, N$, which is often referred to as the *placement operator*. As shown in Figure 5.4, the integer $I(k)$ gives the vertical (or frequency) slot placement for the pulse occupying the k -th horizontal (or time) slot. For example, the placement operator for the pattern in Figure 5.4 would be $\{I(k), k = 1, \dots, 5\} = \{5, 3, 2, 4, 1\}$. Once a placement operator is formed, a hop-coded time-frequency pattern may be generated by Equation (5.3) where the individual pulse frequencies are given by

$$f_k = \Delta f \left[I(k) - \frac{N+1}{2} \right]; k = 1, \dots, N. \quad (5.4)$$

As before, N is the number of subpulses and Δf is the frequency separation between adjacent frequency slots. This method is generally referred to as the linear

frequency allocation algorithm and is commonly used for the relatively narrowband waveforms which will be discussed here. An alternate algorithm which uses logarithmically allocated frequencies is discussed in [23] and is recommended when wideband processing is being used.

Recall from Equation (2.19) that the auto-ambiguity function is a correlation of the transmit waveform with time and frequency shifted versions of itself. Consequently, it is possible (with some restrictions) to estimate the gross ambiguity sidelobe structure of a waveform by studying the auto-correlation properties of its time-frequency pattern. Taking the time-frequency pattern of Figure 5.4 and correlating it with itself, we obtain the pattern of Figure 5.5. In the figure, integers

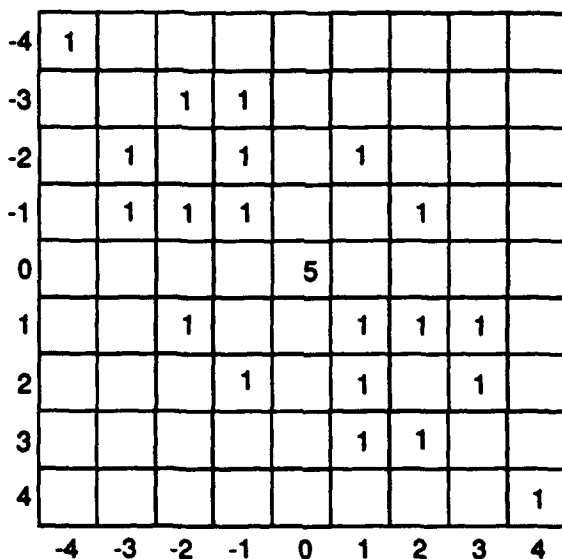


Figure 5.5: Time-Frequency Auto-correlation Pattern

are used to indicate the number of coincident chips for a given time and frequency

shift of the pattern with respect to itself. Note that in the center of the pattern there is a 5 where all chips coincide. This is the case of no shift which corresponds to the mainlobe of the auto-ambiguity surface. Also note, that for any other time and frequency shift there is a maximum coincidence or "hit" of 1. This "minimal intersection" property is highly desirable because it implies that ambiguity volume will be spread so that sidelobe height is minimized. Figure 5.6 shows the ambiguity function resulting from a waveform with the time-frequency pattern of Figure 5.4 where each chip has a duration $T_s = 0.1$ seconds and the chip spacing is $\Delta f = 100$ Hertz. The ambiguity surface is displayed in terms of contours at 3, 6, 10, and 20 dB down from the peak of the map to show that all sidelobes are of equal height with positions corresponding to those predicted by the pattern correlation of Figure 5.5. The usefulness of a minimally intersecting array was first noted by Costas [12]; therefore, such arrays are often referred to as Costas arrays.

Several algebraic constructions have been developed using modulo arithmetic on finite fields to produce time-frequency arrays. Some of the more commonly used constructions are:

1. **Welch Construction [14].** *Let α be a primitive element in the finite field $GF(q)$ where q is a prime number. For a $(q-1) \times (q-1)$ array, place a pulse in the position $(i, j) = (i, \alpha^i \bmod q)$ for $i = 1, \dots, (q-1)$.*
2. **Golomb Construction [14].** *Let α and β be primitive elements in the finite field $GF(q^n)$ where q is a prime number and n is an integer greater than or equal to 1. For a $(q^n - 1) \times (q^n - 1)$ array, place a pulse in the position (i, j)*

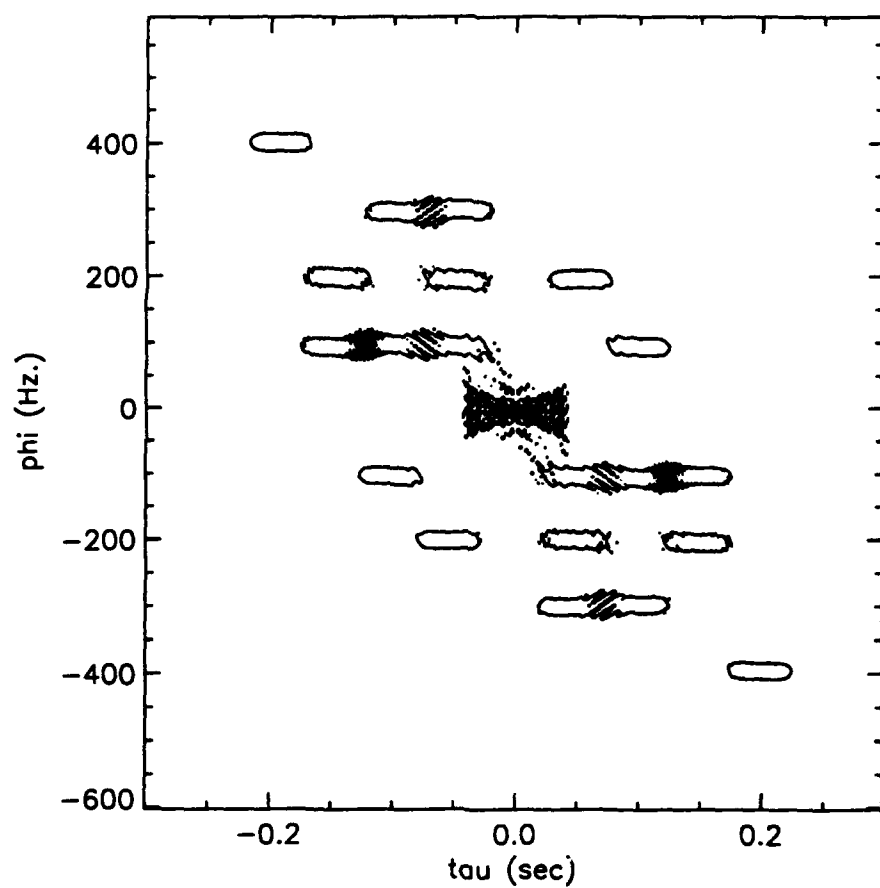


Figure 5.6: Sample Costas Ambiguity Function

if $\alpha^i + \beta^j = 1$ where $i, j = 1, \dots, (q^n - 2)$. If $\alpha = \beta$, then the construction is referred to as the **Lempel construction**.

3. The Linear Congruence (LC) Code [24]. Let q be a prime number. For a $q \times q$ array, place a pulse in the position $(i, j) = (i, (ai) \bmod q)$ for $i = 1, \dots, q$ and $1 \leq a \leq q$.

4. The Quadratic Congruence (QC) Code [21]. Let q be a prime number. For a $q \times q$ array, place a pulse in the position $(i, j) = (i, (i(i + 1)/2) \bmod q)$ for $i = 1, \dots, q$.

5. The Hyperbolic Congruence (HC) Code [22]. Let q be a prime number. For a $q \times q$ array, place a pulse in the position $(i, j) = (i, (a/i) \bmod q)$ for $i = 1, \dots, q$ and $1 \leq a \leq q$.

In the code constructions above, the subpulse index, k , and the placement operator, $I(k)$, have been replaced by time and frequency indices i and j , respectively. Figure 5.7 shows some examples of time-frequency patterns produced by a few of these constructions. Of the constructions listed above, only the Welch and the Golomb produce Costas arrays by the strict definition. The Quadratic Congruence construction produces a modulo description of a parabola on the finite field $GF(q)$ as seen in Figure 5.7(d). Although the QC codes are not full codes—two subpulses often occupy the same frequency slot while others are left empty—their time-frequency patterns are minimally intersecting. The Hyperbolic Congruence construction produces full codes as does the Linear Congruence construction (provided q is not

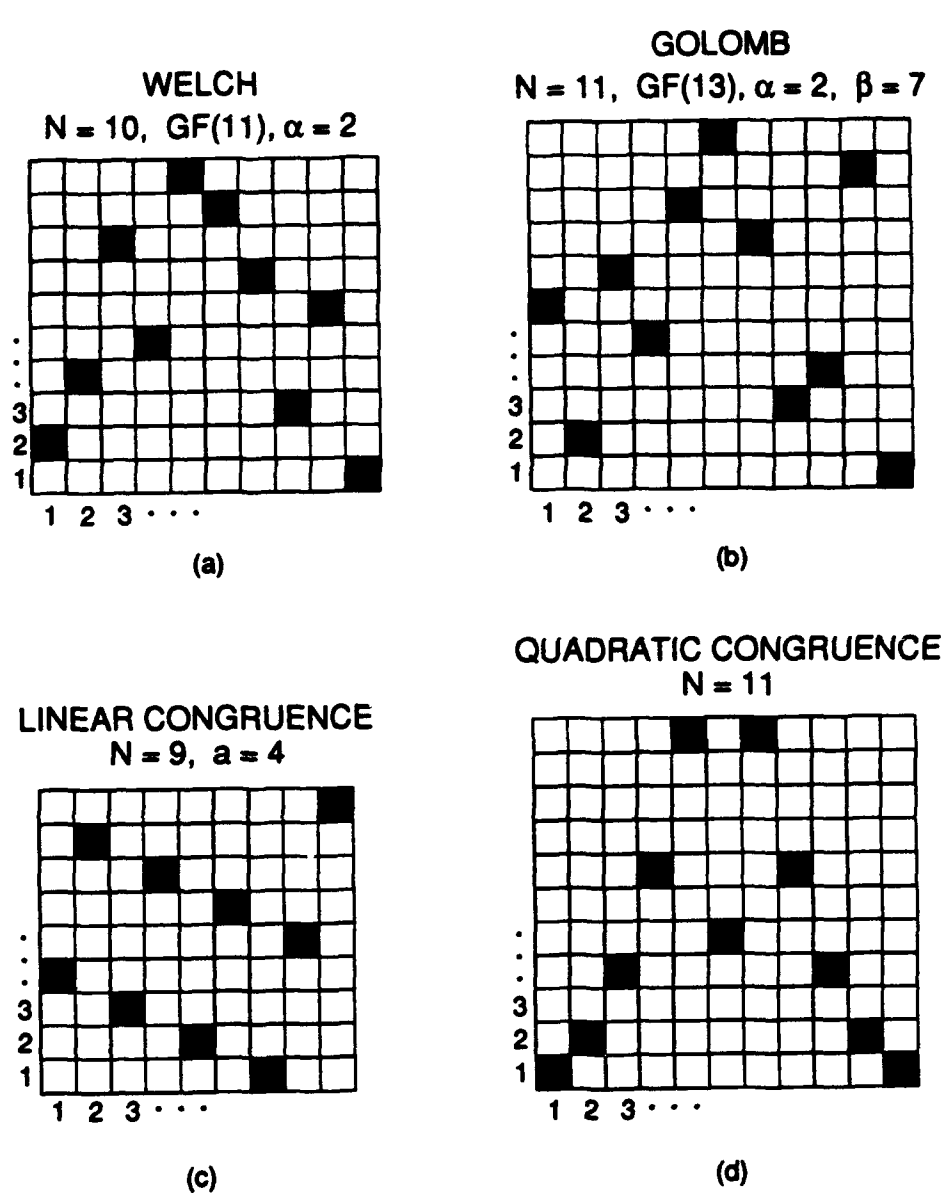


Figure 5.7: Sample Time-Frequency Patterns of Various Constructions

divisible by a); however, neither of these codes are minimally intersecting and thus, do not produce nearly ideal “thumbtack” ambiguity surfaces. LC codes can be thought of as a hop code description of a discrete LFM waveform of slope a on a finite field $GF(q)$ and as such, may be applicable where the LFM would be. HC codes, although less than ideal for auto-ambiguity surfaces do produce desirable cross-ambiguity surfaces, making them useful when UP cross-uncertainty effects are a particular concern.

5.2 The Product of Hit Arrays

As it has been previously shown, it is possible to determine the rough ambiguity structure of a hop-coded waveform by counting the number of subpulse hits occurring in the auto-correlation of its time-frequency pattern. Often this correlation is referred to as an “auto-hit array.” A complete discussion of the validity of using hit arrays may be found in [7]. For the present discussion it is sufficient to state that a waveform’s auto-hit array represents a discrete version of the auto-ambiguity function provided

$$N^2 \ll TW \quad (5.5)$$

where N is the number of subpulses, and T and W are the total signal duration and bandwidth, respectively. In other words, each subpulse must be temporally and spectrally distinct. Likewise, the cross-correlation or “cross-hit array” between two waveforms accurately describes their cross-ambiguity surface if Equation (5.5)

holds for both.

When hit array use is valid, the basic structure of the uncertainty product function of two waveforms may be determined by taking an element-by-element product of their two auto-hit arrays [18]. Recall that the expected output of the UP receiver of Equation (4.4) involved both auto-uncertainty and cross-uncertainty function terms. Therefore, it is also necessary to study the structure of the cross-hit array to estimate the usefulness of any pair of codes.

Ideally, one would like to have a minimum number of hits in both the product of auto-hit arrays and the cross-hit array to optimize receiver performance. However, as the previous section demonstrated, generally a waveform does not have both desirable auto- and cross-ambiguity properties. A reasonable approach is to study the problems of auto-uncertainty product minimization and cross term minimization separately. If a sufficient clear area may be established, it is preferable to use two waveforms which have good a minimum hit array product. When this is not possible, two signals with a good cross-hit array may be more desirable.

The simplest minimal product code is a discretized version of the up/down chirp combination used previously. For example, Figure 5.8 shows the hit array analysis for the combination of up and down 5-chip steppedLFMs. Note that the hit array product is optimal, even though this combination can produce severe virtual scattering effects in the presence of two or more point scatterers, as was shown for the continuous case in Section 4.3. Clearly, the best choice of waveforms to minimize uncertainty-function product effects would be two waveforms with minimally

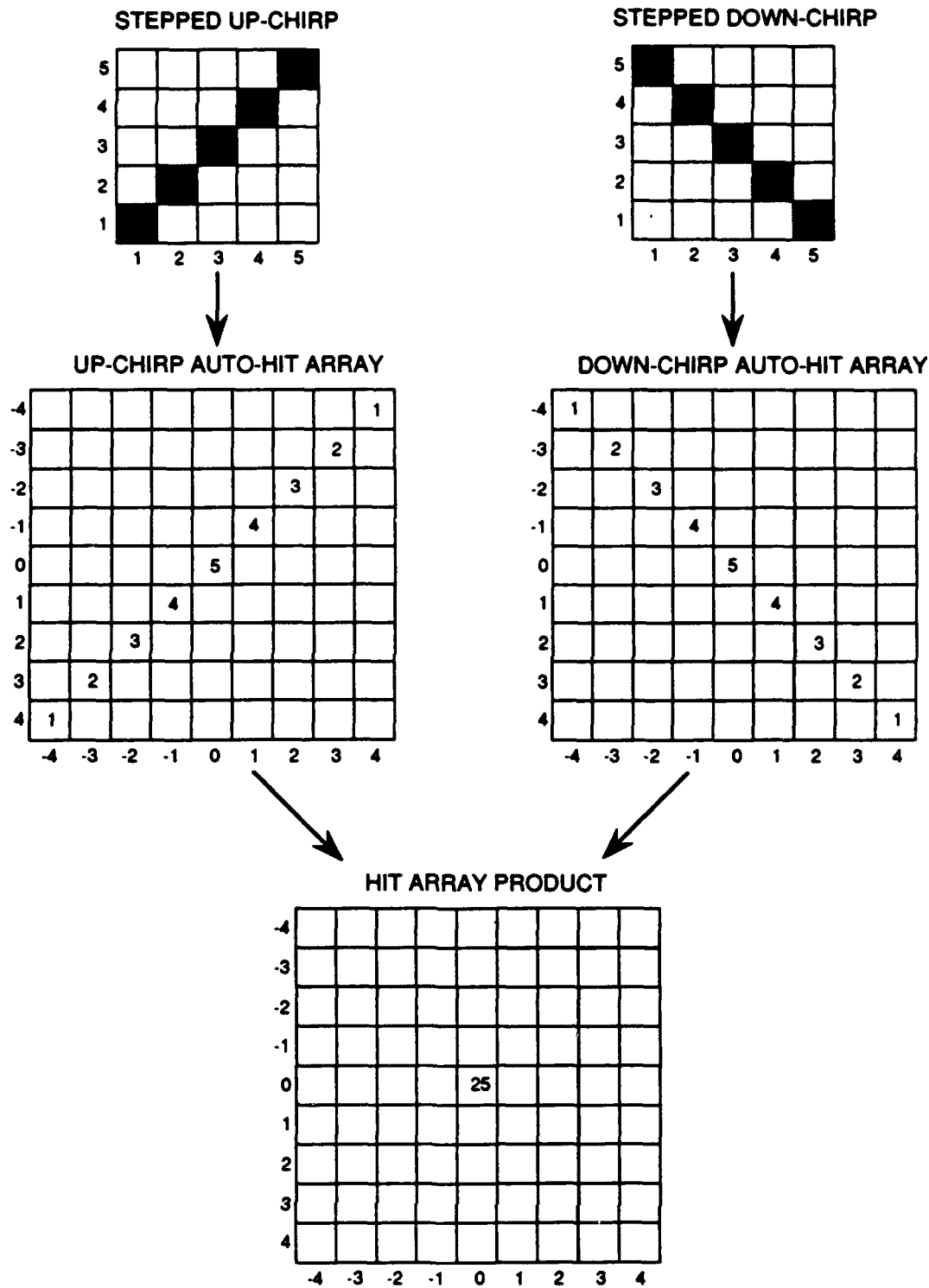


Figure 5.8: Hit Array Analysis for Up/Down Stepped LFM

intersecting auto-hit arrays and minimal hit array products. Unfortunately, these two goals are difficult to achieve simultaneously. To illustrate this fact, Tables 5.1-5.3 list constructions for pairs of Welch, HC, and Golomb codes which produce minimal hit array products. Note that the hyperbolic codes of Table 5.2 [18] tend to have fewer product hits than the Welch codes of Table 5.1 [25] or the Golomb codes of Table 5.3. Unfortunately, since HC codes are not Costas arrays, hit array products may have magnitudes greater than 1, whereas Welch and Golomb codes are assured to have products of maximum height 1.

The consideration of cross-uncertainty effects may be equally influential in the selection of UP waveforms if a sufficient clear area is not achievable. As mentioned above, these effects may be studied by considering the cross-hit array of the two receiver waveforms. In this regard, linear congruence codes seem optimal in that their cross-hit arrays have a maximum of 1 hit as illustrated in Figure 5.9 for the up/down chirp combination which contains LC codes of order one. Slightly less desirable are the QC and HC codes which have a maximum of 2 cross-uncertainty hits. The least desirable codes in this regard are the Costas codes which produce a maximum of $(N - 1)/2$ hits.

5.3 Code Density

In the previous section, hit array methods were introduced as a tool to analyze the performance of hop-coded waveform pairs, with the assumption that each subpulse was temporally and spectrally distinct. If the code density, i. e. the

Table 5.1: Welch Construction Minimum Hit Array Pairs

| Prime | N | Welch Pairs (α_1, α_2) | # Hits |
|-------|----|---|--------|
| 5 | 4 | (2,3) | 6 |
| 7 | 6 | (3,5) | 14 |
| 11 | 10 | (2,8), (6,7) | 34 |
| 13 | 12 | (2,7), (6,11) | 62 |
| 17 | 16 | (3,6), (3,12), (5,7) (10,12), (11,12), (11,14) | 114 |
| 19 | 18 | (3,15) | 134 |
| 23 | 22 | (7,15) | 188 |
| 29 | 28 | (3,21) | 320 |
| 31 | 30 | (21,24) | 386 |

Table 5.2: HC Construction Minimum Hit Array Pairs

| Prime | Hyperbolic Pairs (a_1, a_2) | # Hits |
|-------|---------------------------------|--------|
| 7 | (1,4), (2,4), (3,5), (3,6) | 0 |
| 11 | (1,5), (2,8), (3,9), (6,10) | 7 |
| 17 | (1,9), (8,16) | 25 |
| 19 | (6,11), (8,13) | 38 |

Table 5.3: Golomb Construction Minimum Hit Array Pairs

| Prime | N | Golomb Pairs $(\alpha_1, \beta_1) \times (\alpha_2, \beta_2)$ | # Hits |
|-------|----|---|--------|
| 11 | 9 | $(2,7) \times (2,8), (2,7) \times (6,7), (2,8) \times (6,8),$ $(6,7) \times (6,8), (7,2) \times (7,6), (7,2) \times (8,2),$ $(7,6) \times (8,6), (8,2) \times (8,6)$ | 24 |
| 13 | 11 | $(2,6) \times (2,11), (2,6) \times (7,6), (2,11) \times (7,11),$ $(6,2) \times (6,7), (6,2) \times (11,2), (6,7) \times (11,7),$ $(7,6) \times (7,11), (11,2) \times (11,7)$ | 36 |
| 17 | 15 | $(3,5) \times (3,7), (3,5) \times (6,5), (3,7) \times (6,7),$ $(5,3) \times (5,6), (5,3) \times (7,3), (5,6) \times (7,6),$ $(6,5) \times (6,7), (7,3) \times (7,6)$ | 72 |
| 19 | 17 | $(2,3) \times (13,10), (3,2) \times (10,13)$ | 98 |
| 23 | 21 | $(7,15) \times (11,21), (10,20) \times (11,21),$ $(15,7) \times (21,11), (20,10) \times (21,11)$ | 154 |
| 29 | 27 | $(8,11) \times (14,26), (8,11) \times (19,27),$ $(8,11) \times (26,14), (8,11) \times (27,19),$ $(11,8) \times (14,26), (11,8) \times (19,27),$ $(11,8) \times (26,14), (11,8) \times (27,19)$ | 270 |

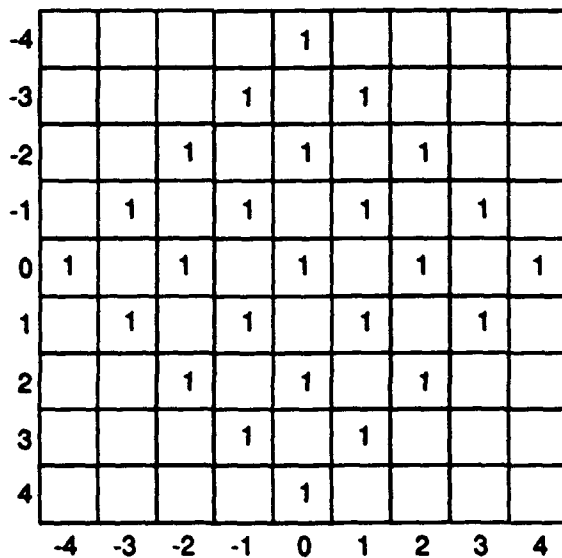


Figure 5.9: Hit Array Analysis for Up/Down Stepped LFM

number of subpulses per the total duration and bandwidth, is increased, individual subpulses are no longer distinguishable, making hit array analysis invalid. In other words, this occurs when

$$N^2 \gg TW. \quad (5.6)$$

This situation does not automatically imply poor auto-ambiguity surfaces with undesirable uncertainty product effects. If one chooses Costas codes with auto-hit arrays which have hits distributed evenly throughout the array, the resulting ambiguity functions will possess fairly level pedestals with no dominant sidelobes. Figure 5.10 is a illustration of this effect where the ambiguity function of a Golomb code is displayed where the finite field $GF(29)$ was used with primitive elements $\alpha = 8$ and $\beta = 11$ allocated over a total duration of $T = 0.5$ seconds and a bandwidth of $W = 400$ Hertz. The reasoning behind this is that if two waveforms with flat pedestals are combined, the resulting UPF will also have a flat pedestal which is of a higher average level than the UPF sidelobes of the constructions previously discussed. The use of such a pair of codes is suggested when it's especially important to lessen the probability of obtaining strong virtual scatterers on any one realization.

A final method for selecting two hop codes again involves the use of two Costas codes. Although all of the code constructions listed in Table 5.1 and Table 5.3 produce Costas arrays, a study of all the hit arrays for a given code order reveals that the auto-hit arrays of certain codes will tend to have hits more densely distributed along either the horizontal axis, the vertical axis, or either of the di-

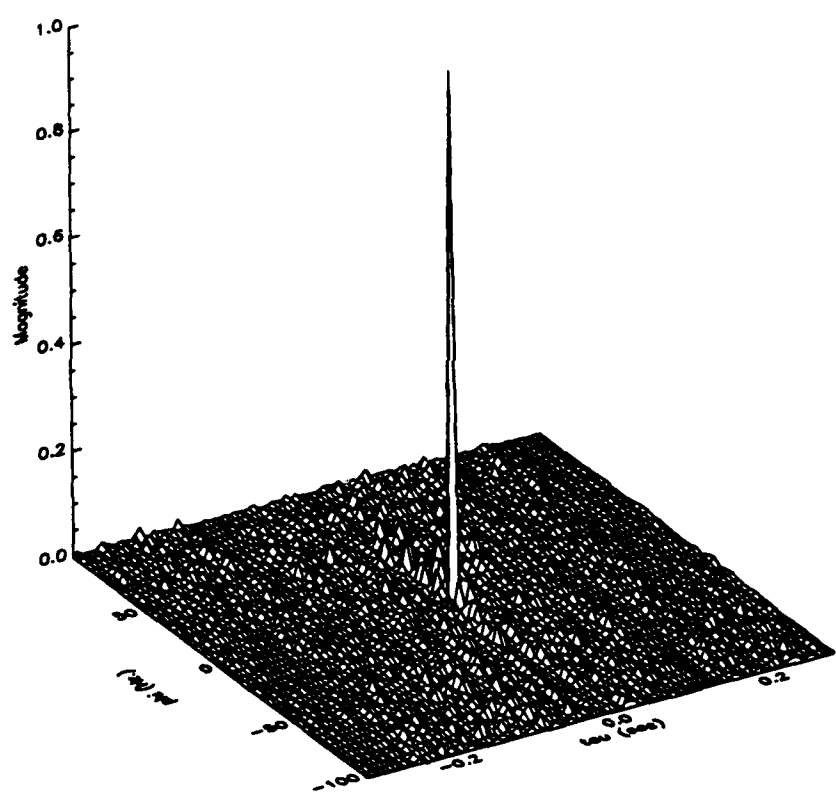


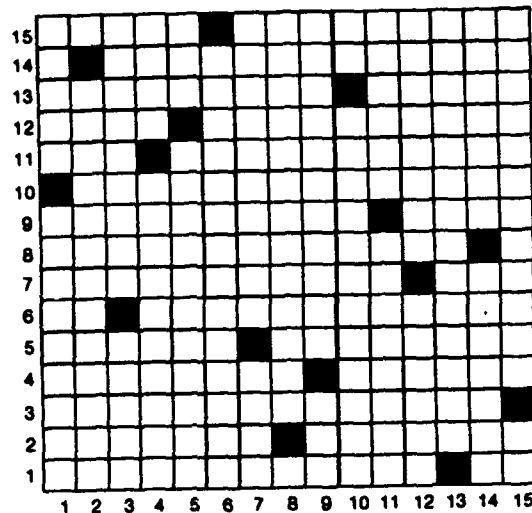
Figure 5.10: High Density Hop Code Ambiguity Function

agonals of the array. For example, Figure 5.11 displays the pattern for a code of Golomb construction on $GF(17)$ with $\alpha = 3$ and $\beta = 6$ along with its corresponding auto-hit array where the majority of the hits are aligned along the diagonal of the array. A code such as this will tend to have a pedestal with more sidelobe volume distributed along the diagonal axis. In this instance we would like to generate a second waveform whose pedestal is oriented perpendicular to the first. This may be accomplished by taking the original code's time-frequency pattern and rotating it 90 degrees. The resulting pattern is of course still a Costas array—in this case on $GF(17)$ with $\alpha = 3$ and $\beta = 3$ (i.e., a Lempel code)—and has an auto-hit array which is a 90 degree rotation of that of the original code. Even though a hit array analysis is not valid because of the high code density, the hit arrays of the two codes do give an indication that these perpendicular codes will have pedestals oriented in opposing directions, implying lower UPF sidelobes.

5.4 Application Specific Design

Proper choice of UP receiver waveforms depends primarily on the expected structure of the scattering function to be interrogated. In particular, the problems associated with using a bistatic sonar UP receiver for channel identification will be considered here. Factors which play key roles in waveform selection are the number and density of the individual point scatterers and the degree of stationarity of the scattering process.

Clearly, in the trivial case where the scattering function consists of only the



AUTO-HIT ARRAY

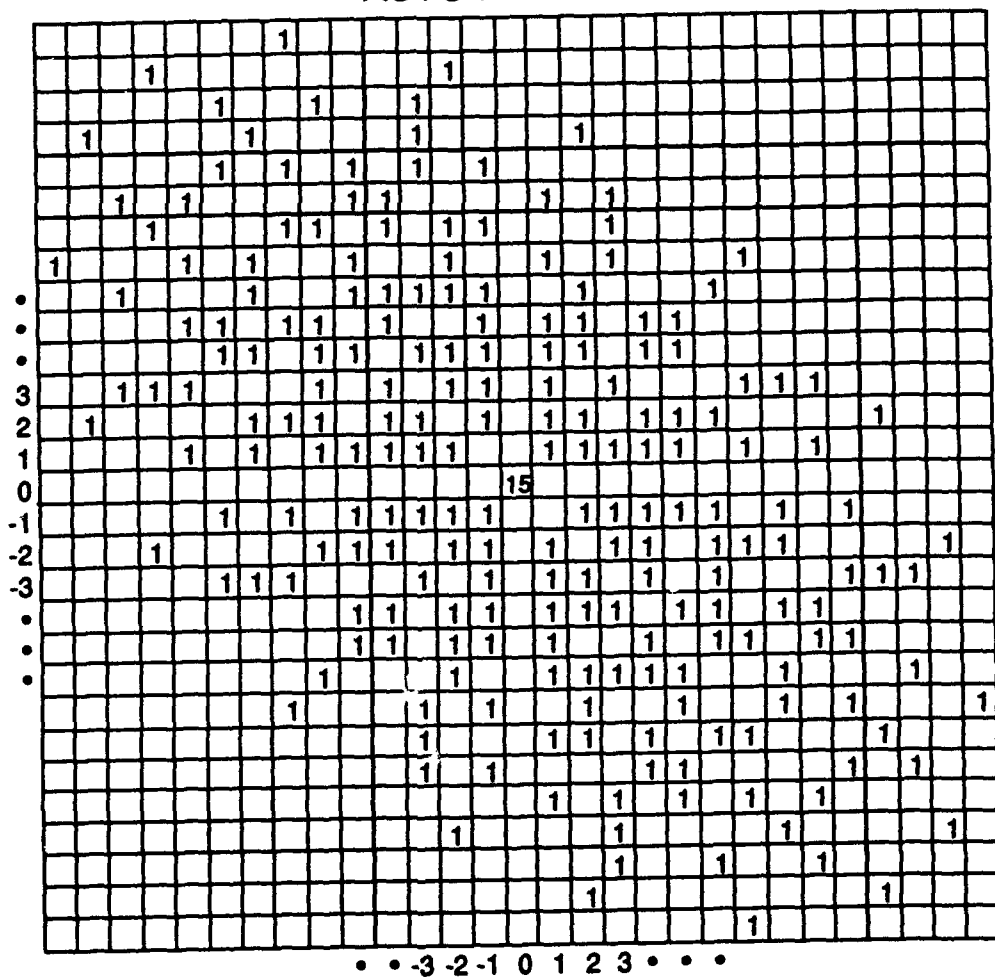


Figure 5.11: Golomb Time-Frequency Pattern and Associated Auto-Hit Array

direct path response from the source to the receiver with no multipath receptions, nearly any pair of codes would be sufficient provided that their UPF exhibits the desired mainlobe resolution. In this case, either the combination of up and downLFMs or long and short CWs would provide a completely unambiguous estimate of the scattering process with effectively no sidelobe interference.

Direct path transmission in a benign medium is an ideal situation of very little interest. More likely are the cases where at least one (and possibly several) multipaths are present at the receiver. Multipath receptions occur when multiple propagation paths exist between the source and the receiver. Commonly, multipath is evident when propagation is bounded within a surface or deep water duct or in shallow water where multiple reflections from the bottom and/or surface are often present [26]. These multiple reflections generally exhibit a limited spread in both range-delay and Doppler shift so that a sufficiently large clear area may be established about the scattering process. As mentioned previously, multiple returns can cause virtual scattering effects. These effects may be manifested as distinct peaks in the receiver output when combinations of CWs or FMs are used, but will decay as convergence is achieved, leaving an accurate channel measurement. Proper receiver convergence is most readily obtained when both the transmitter and receiver platforms are fixed and the multipath mechanisms remain relatively constant for an extended period of time. In such situations CW or LFM combinations are recommended to obtain a clutter-free scattering function estimate.

Unfortunately, it is usually impossible to obtain the ideal measurement condi-

tions described above. When obtaining open ocean measurements it is very difficult to maintain stationary platforms for an extended period of time. In these cases, it is preferable to use a Costas minimal hit array product waveform pair which provides better channel estimates on a single interrogation than do the CW or LFM pairs. Furthermore, when the path lengths of the multipath echos are very close to that of the direct path, signal range-delay resolution may be maintained with sufficient signal bandwidth. This is not the case with the LFM's where the close temporal proximity of two returns will result in virtual scatterers which are nearly at the same Doppler as the true returns (refer to Figure 4.6).

Usually, channel measurements will consist of only the direct path and a few multipaths. In cases of dense scattering where a large number of multipaths are present (or for a large quantity of reflections in the monostatic case), any pair of waveforms will have difficulties. In these instances, the CW and LFM combinations will produce virtual scatterers which fill the range-Doppler plane. For hop code pairs, initially self-clutter produced by the UPF sidelobes can mask the returns, much as is the case in matched filter processing. However, it should be noted that if stationarity is maintained, the UPF will converge to an accurate scattering function estimate, while the matched filter will remain masked by self-clutter.

Chapter 6

Open Ocean Surface Scattering Function Estimation

A series of open ocean, high-frequency, surface scattering experiments were conducted by the Applied Physics Laboratory, University of Washington (APL/UW) during January-February 1992 off the coast of California. The tests involved the use of the Marine Physical Laboratory's (MPL) Floating Instrumentation Platform (FLIP) as a stable base for conducting forward and backward acoustic surface scattering experiments. These measurements were performed using waveforms specified by both APL/UW and the Applied Research Laboratory of the Pennsylvania State University (ARL/PSU). Included in the ARL/PSU waveforms was a signal designed for UP receiver measurement of forward surface scattering. This chapter presents an overview of the UP experiment, discusses UP waveform selection criteria, and presents results from both UP and matched filter (one channel) processing of the data.

6.1 Experiment Overview

The forward scattering experiment involved the transmission of two time concatenated hop-coded waveforms through a 1 km channel. The planned geometry for this experiment is shown in Figure 6.1. A goal of this experiment was to obtain an estimate of range and Doppler spread occurring in both the direct path and

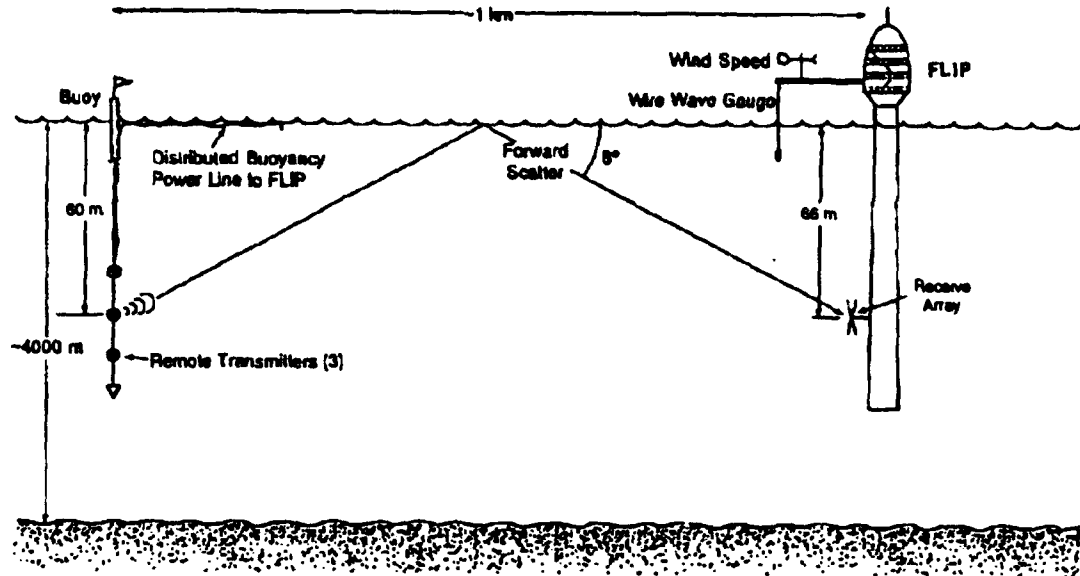


Figure 6.1: FLIP Forward Scattering Geometry

surface multipath as they pass through the channel. Transmission originated from a spherical source suspended from a buoy at a depth of 60 meters, with reception occurring on a small planar array mounted to the hull of the FLIP at a depth of 66 meters. Because other experiments were being conducted simultaneously, the receive array was tilted up at an angle of 20 degrees above horizontal. An analysis of the geometry using the method of images [27] predicts that the expected direct path length between the source and the receiver is 1000.02 meters, and that the surface bounce path length is 1007.9 meters. The angles of arrival for the direct and surface paths would be 0.34 degrees and 7.18 degrees above the horizontal, respectively. The vertical receive beam pattern for the array is shown in Figure 6.2. A 20 degree upward tilt of the array would cause the direct and surface paths to

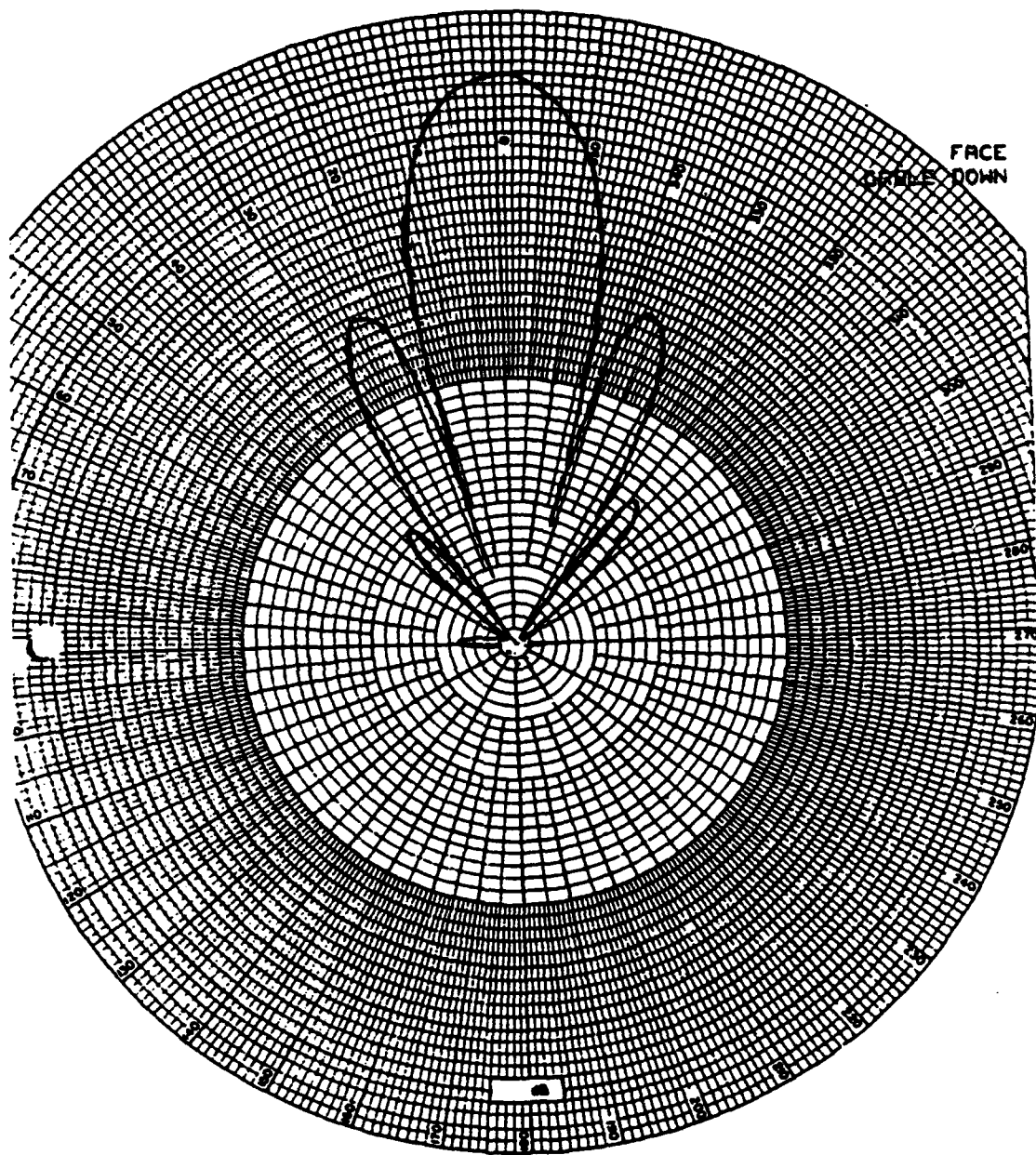


Figure 6.2: FLIP Vertical Receive Beam Pattern

arrive at 340.3 and 347.2 degrees w. r. t. the MRA of the array, yielding attenuations approximately 23 dB and 9 dB down, respectively.

6.2 Waveform Selection

In Chapter 5, many factors were discussed for choosing appropriate UP waveforms, with scattering function density being a key consideration in this process. In the FLIP forward scattering experiment, a relatively simple scattering process was expected consisting of a direct path and a single surface bounce path. No bottom reflections would be observed due to the depth of the ocean at the test site. Recall that the expected path lengths of the two receptions were calculated to be 1000.02 m and 1007.9 m, implying a delay difference of only 5.25 msec. In addition, good resolution in both range and Doppler were required to measure any subtle time and frequency spreading caused by the channel. These requirements dictated the use of waveforms with appreciable duration and bandwidth. Accordingly, the duration and bandwidth of each waveform were chosen to be 200 msec and 450 Hz, respectively, yielding a mainlobe resolution of 2.95 m in range (1.96 msec) and 4.43 Hz in Doppler shift.

Because the expected support of the scattering function was so small, it was determined that a clear area 100 msec in range-delay and 100 Hz in Doppler would be sufficient to eliminate cross-uncertainty effects. Two Costas codes of 27 subpulses each were chosen in an attempt to obtain a highly resolvent UPF. Both codes were of the Golomb construction, with the second being a 90 degree rotation

of the first. In particular, the first code was formed on $GF(29)$ with $\alpha = 8$ and $\beta = 11$ and the second on $GF(29)$ with $\alpha = 14$ and $\beta = 26$. The time-frequency patterns for the codes are shown in Figure 6.3. Recall from Table 5.3 that these codes form a minimal auto-hit array pair, making them good choices for minimizing UPF sidelobes. The auto-ambiguity function of the first waveform and the UPF of the two codes are displayed in Figures 6.4 (a) and (b), respectively.

6.3 Forward Scattering Function Estimation

Using the test configuration shown in Figure 6.1, a total of 24 acoustic transmissions (or pings) of the UP waveform were recorded for subsequent processing. Data was recorded for 600 msec during each cycle and there were 4 seconds between transmissions.

6.3.1 Receiver Modifications

Figure 6.5 displays the received time series for Ping 1 and its corresponding spectrum. Unfortunately, one can see by comparing the envelope of the first waveform to that of the second that the first waveform is considerably shorter. This was caused by improper range gating of the received signal.

As shown in Figure 6.1, a positively buoyant power line connected the buoy and the FLIP. This cable assured that the maximum distance between the source and the receiver would be 1 km. However, ocean currents sometimes caused the buoy and the FLIP to drift closer together than the prescribed 1 km. Data recording at the receiver commenced 500 milliseconds after the beginning of transmit. This

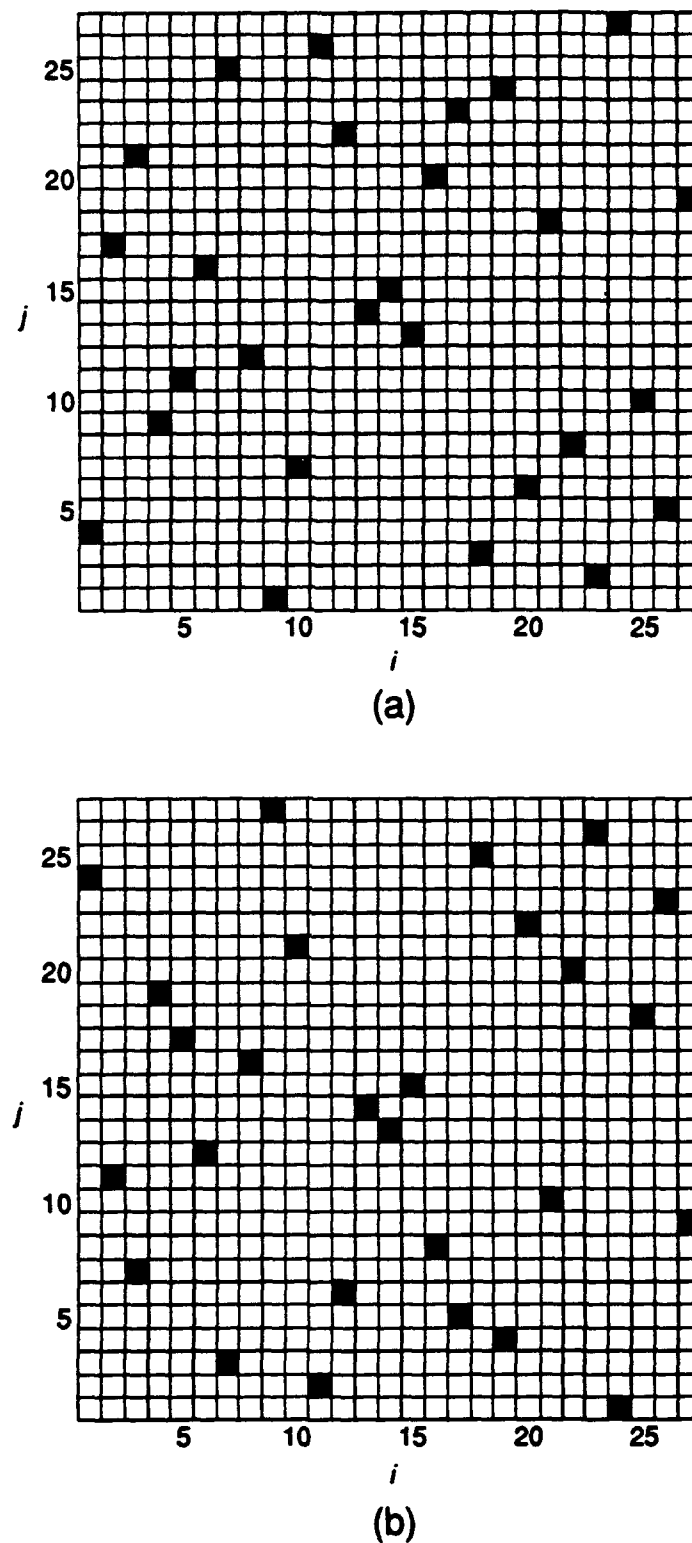
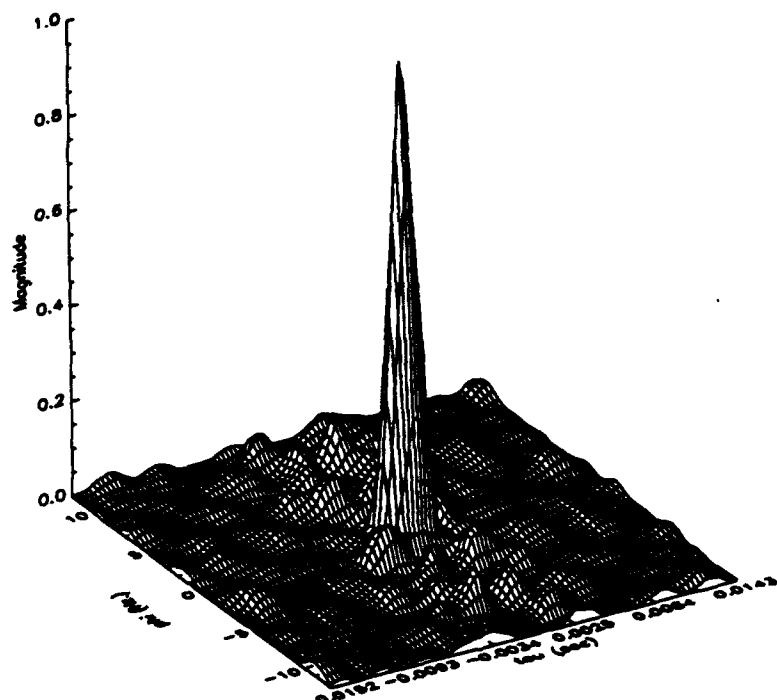
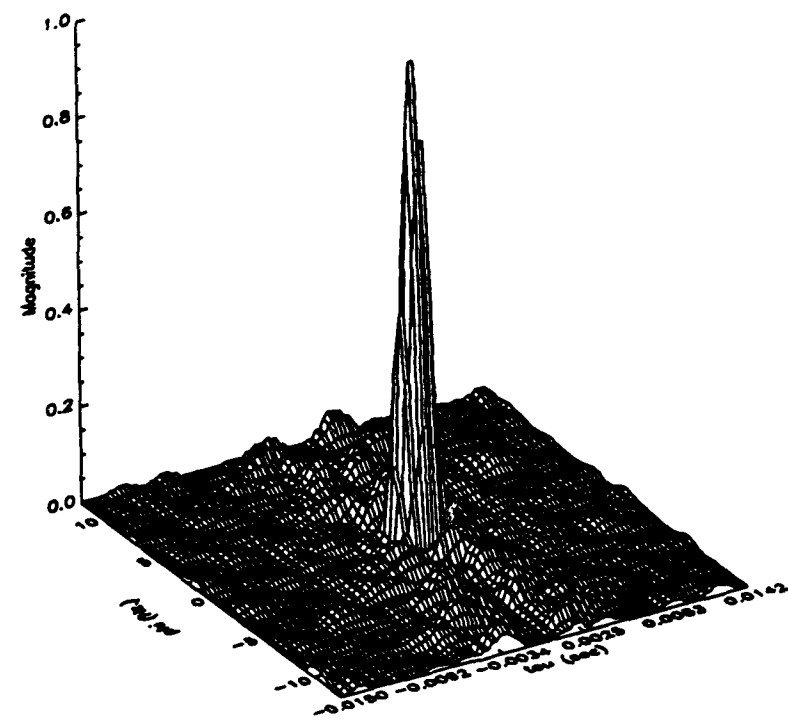


Figure 6.3: FLIP Waveform Time-Frequency Patterns



(a)



(b)

Figure 6.4: FLIP Waveform Functions: (a) Waveform 1 Ambiguity Function, (b) Uncertainty Product Function

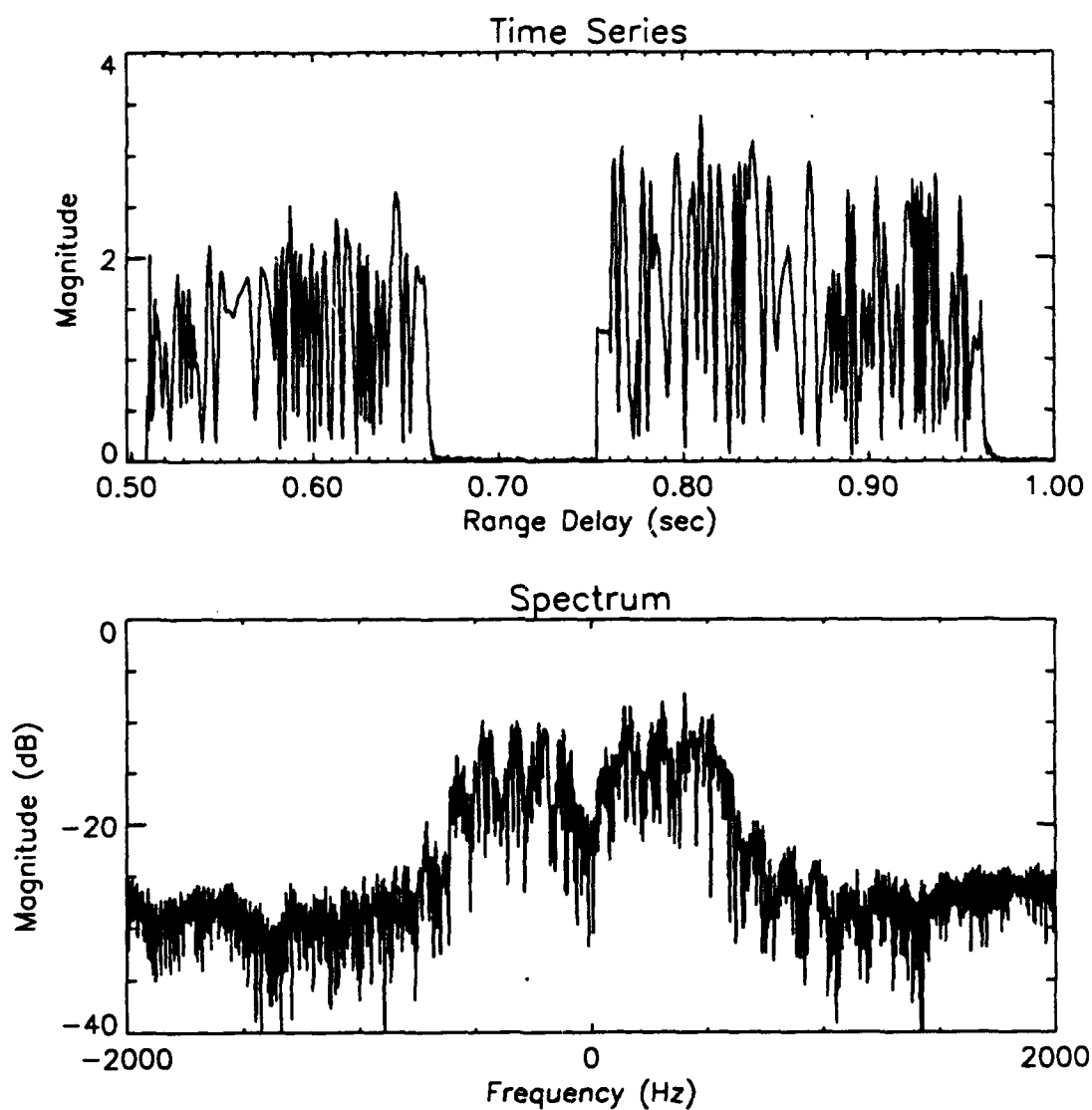
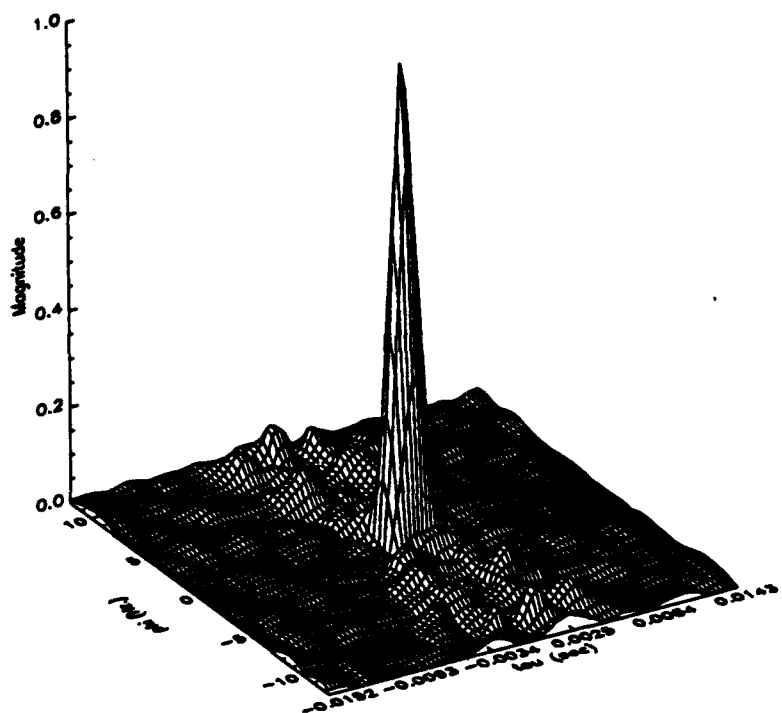


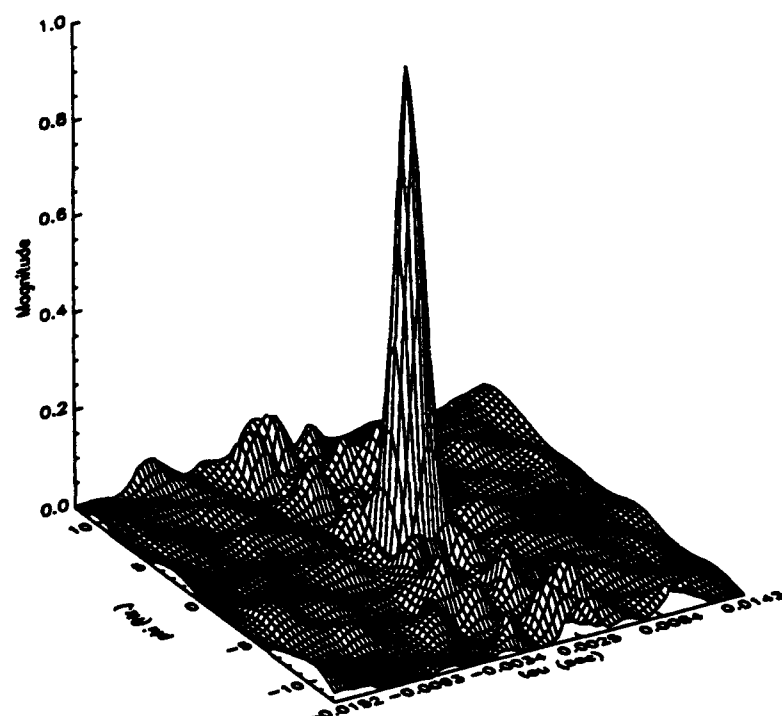
Figure 6.5: FLIP Ping 1 Time Series and Spectrum

delay allowed the source and receiver to be as close as 750 meters apart and still capture the entire waveform. Returning to the time series of Figure 6.5, we see that the leading edge of the second hop code arrives at approximately 0.753 seconds after transmit. This delay corresponds to a delay of 0.453 seconds for the first pulse, yielding a range of 680 meters. Recalculation of the expected surface path length using this range resulted in a path difference of 11.5 meters. Angles of incidence on the receive array face for the direct and surface bounce paths were recalculated as 0.5 degrees and 10.5 degrees, respectively.

Approximately the first eight subpulses of the first waveform were not recorded due to improper gating. In order to form accurate replicas for matched filtering in the first waveform's branch of the receiver, it was determined that only subpulses 9–27 should be used. Although this shorter waveform results in a Doppler resolution of 6.3 Hz, much of the resolution is regained when the product of the matched filter outputs is taken in the UPF. These effects are illustrated with the auto-ambiguity function of the truncated first channel waveform and the resulting UPF in Figures 6.6 (a) and (b). It should also be noted that the "dead time" appended to the front of the second waveform must also reflect the difference in the first signal's length to assure proper range and Doppler alignment of the two channels.



(a)



(b)

Figure 6.6: FLIP Truncated Waveform Functions: (a) Waveform 1 Ambiguity Function, (b) Uncertainty Product Function

6.3.2 Phase Plane Motion

Initially, each of the received pings was matched filtered using each waveform replica separately. Figure 6.7 shows the result of match filtering the modified first waveform against the received time series of Ping 1 (Figure 6.5). The two distinct peaks are returns from the direct path and surface bounce path, which were seen in all pings for each of the matched filter channels. However, the level and position of the two peaks changed somewhat from ping to ping. Figure 6.8 shows the range of the direct path return using the first waveform. Note the periodic variation in the direct path length. Similar measurements of the Doppler centroid for each ping exhibit the same pattern and period, but 90 degrees out of phase with the range measurements.

The exact cause of the motion in the direct path transmission is not known, but it is hypothesized that the motion may be due to motion of the FLIP, on which the receiver was mounted. Figure 6.8 shows that the average excursion of the motion is approximately 0.75 meters with a period of about 5 pings (or 20 seconds.) Discussions with Peter Dahl of APL/UW revealed that swell would normally cause the FLIP to pitch toward and away from the buoy with a period between 20 and 25 seconds [28]. Because the horizontal range between the source and the receiver is much larger than their offset in depth, only motion in the horizontal direction could produce the range variation shown in Figure 6.8.

The underlying goal of the experiment was to measure range and/or Doppler spread in the direct path and surface bounce arrivals. The ensemble average formed

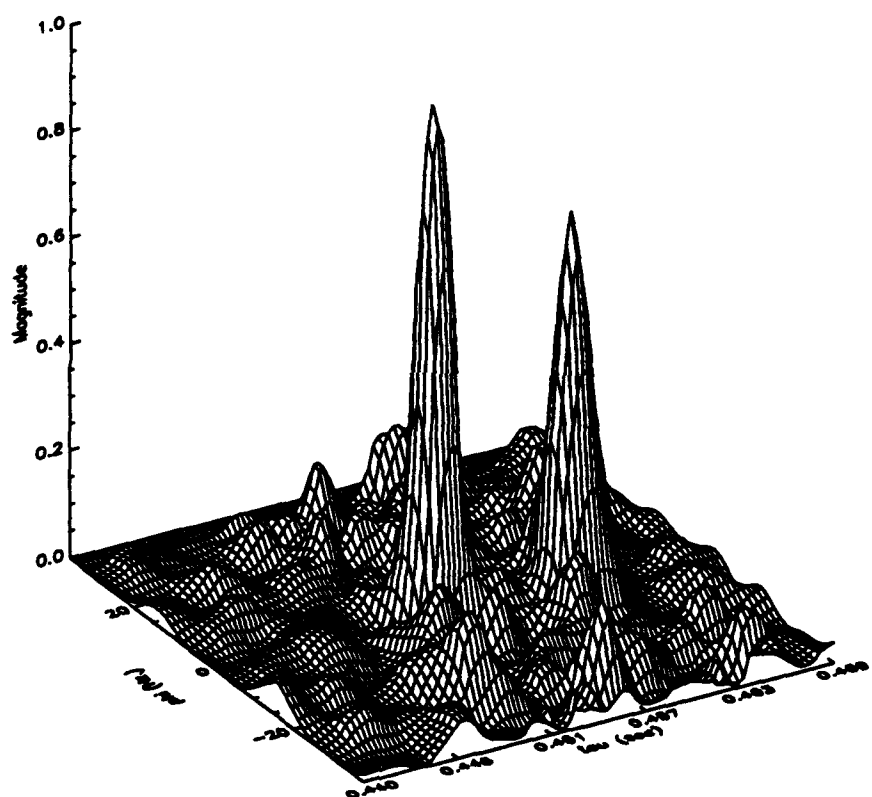


Figure 6.7: FLIP Ping 1 First Channel Matched Filter Output

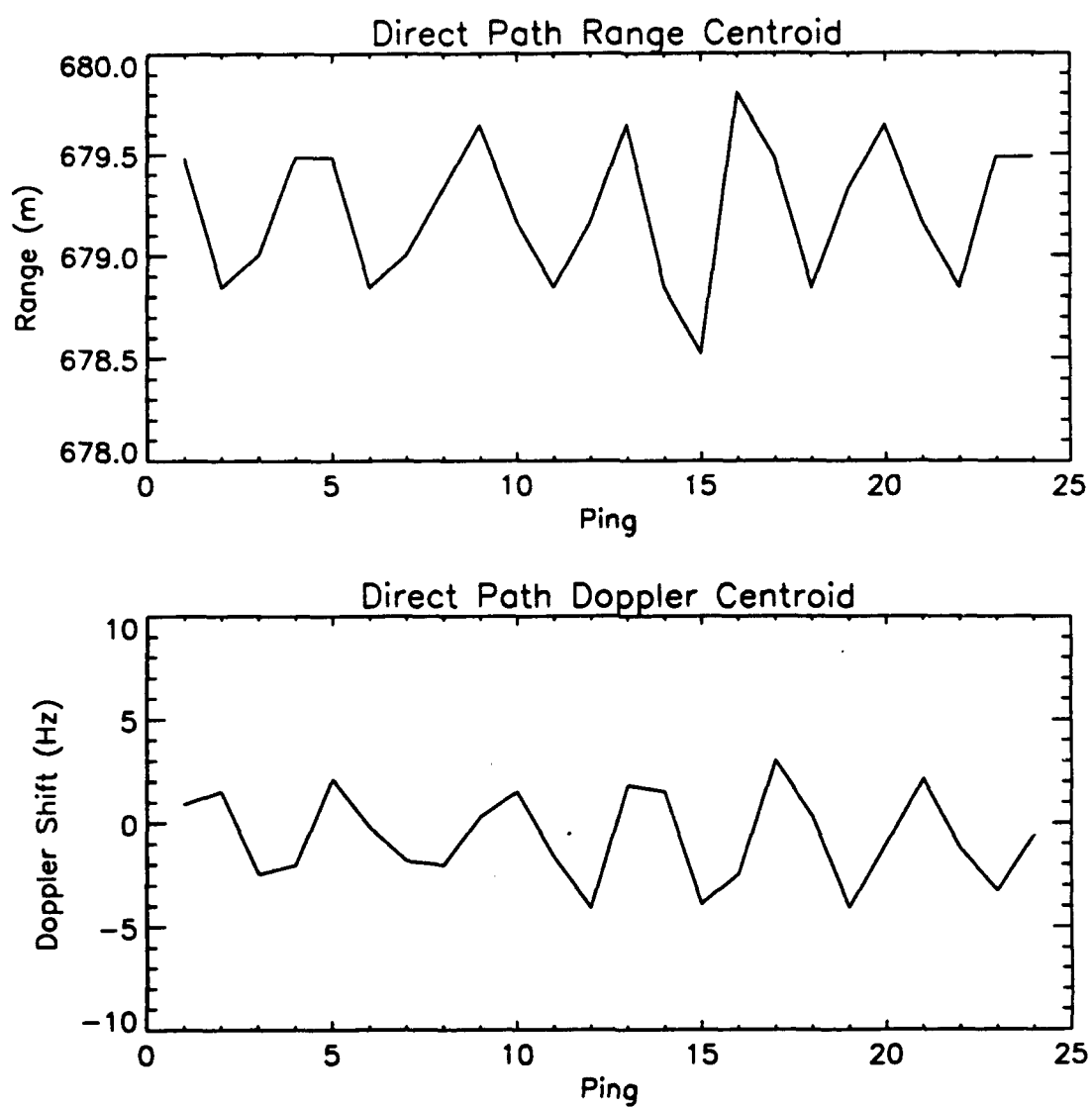


Figure 6.8: Direct Path Range and Doppler Positions

by averaging the uncertainty product receiver outputs indicates range and Doppler spread for both the direct path and the surface bounce path, as illustrated by comparing Figures 6.9 and 6.10. Figure 6.9 is a plot of the UPF showing contours at -3, -6, and -10 dB down from the peak. Figure 6.10 shows the 24 ping average of the UP receiver outputs. Range and Doppler spread are clearly evident when Figure 6.10 is compared to the UPF of Figure 6.9. However, this spreading is due, primarily, to motion of the receiver and/or transmitter between pings.

Range and Doppler spread associated with propagation scattering properties of the medium are of interest. To investigate the medium induced spread, one must correct for the receiver's motion prior to averaging UP outputs. In the absence of ground truth position data, this may be accomplished by aligning each UP output so that the centroids of the direct path returns for all pings coincide. We are also interested in spreading of the surface bounce path. In this case, each UP output must be aligned so that the surface returns coincide. The aligning of UP receiver outputs prior to averaging will be referred to as reregistration, and is designed to correct for motion between the source and the receiver and Doppler shift induced by the surface wave motion.

6.3.3 Uncertainty Product Receiver Processing

The 24 ping ensemble average of reregistered direct path returns is shown in Figure 6.11. Only the contours down from the peak in the direct path return are shown. The mean square spread of the direct path return was estimated for both

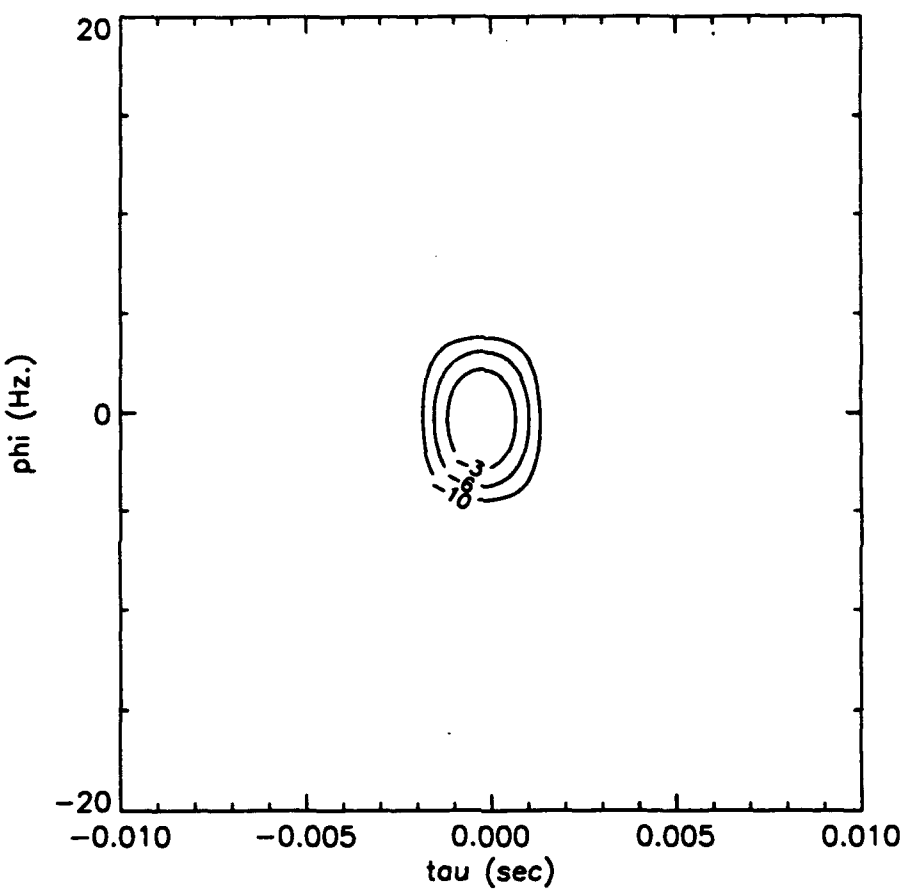


Figure 6.9: FLIP Uncertainty Product Function Contour Map

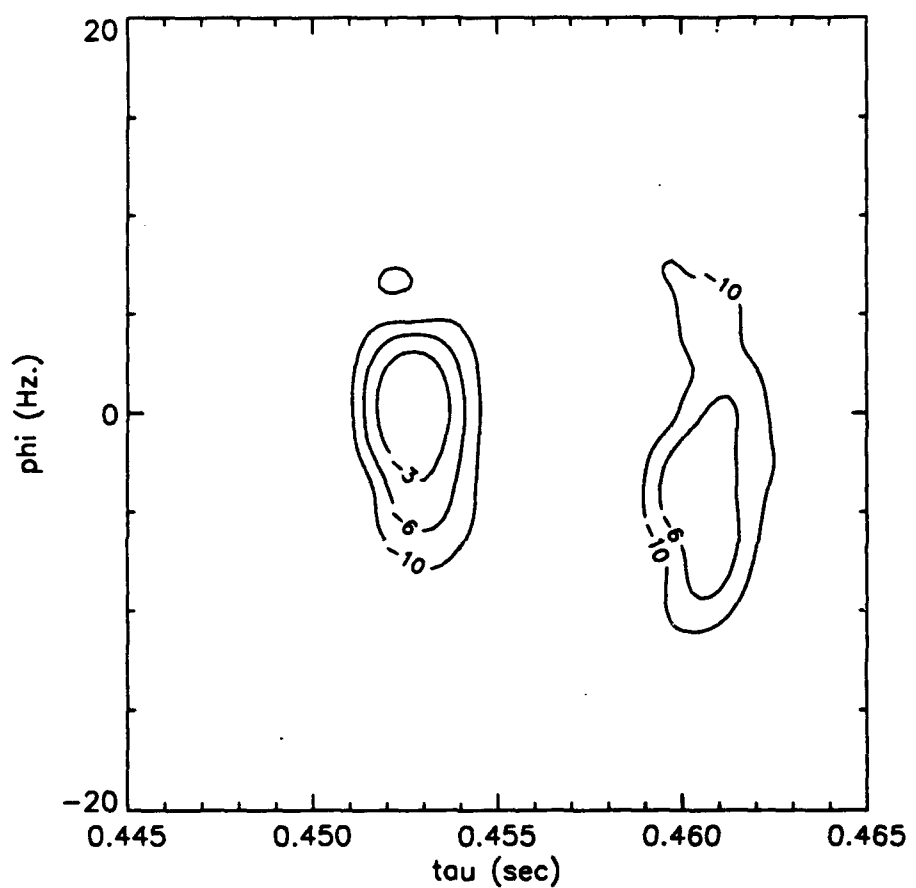


Figure 6.10: FLIP Uncertainty Product 24 Ping Ensemble Average

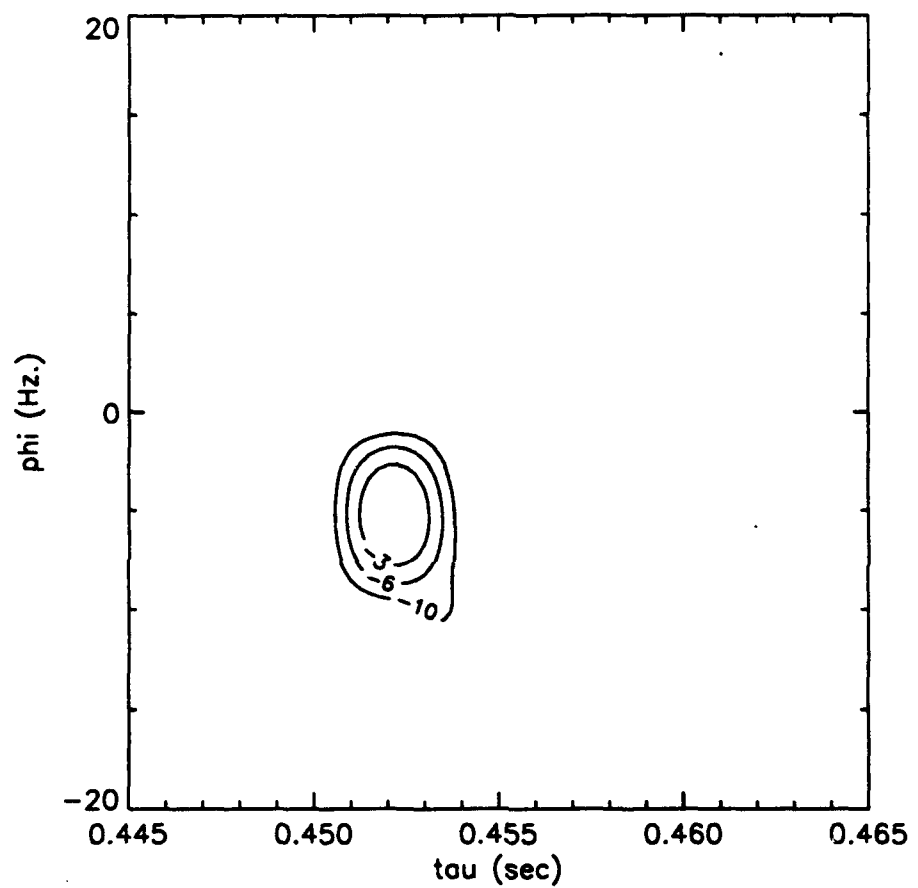


Figure 6.11: Direct Path Reregistered Uncertainty Product Receiver Ensemble Average

range and Doppler using the N points, $\rho_r(\tau_i, \phi_i)$, above the -10 dB contour as

$$\sigma_\tau^2 = \frac{\sum_{i=1}^N (\tau_i - \mu_\tau)^2 w_i}{\sum_{i=1}^N w_i} \quad (6.1)$$

and

$$\sigma_\phi^2 = \frac{\sum_{i=1}^N (\phi_i - \mu_\phi)^2 w_i}{\sum_{i=1}^N w_i} \quad (6.2)$$

where

$$w_i = \rho_r(\tau_i, \phi_i) \quad (6.3)$$

and the mean values are calculated as

$$\mu_\tau = \frac{\sum_{i=1}^N \tau_i w_i}{\sum_{i=1}^N w_i} \quad (6.4)$$

and

$$\mu_\phi = \frac{\sum_{i=1}^N \phi_i w_i}{\sum_{i=1}^N w_i} \quad (6.5)$$

The mean square spreads were also calculated for the UPF of Figure 6.9. The rms spread in the direct path arrival relative to the UPF resolution, $\sigma_{\tau-dp}$, was obtained by taking the square root of the difference between the direct path and UPF mean square measurements, i. e.

$$\sigma_{\tau-dp} = \sqrt{\sigma_\tau^2 - \sigma_{\tau-UPF}^2} \quad (6.6)$$

and

$$\sigma_{\tau-dp} = \sqrt{\sigma_{\tau}^2 - \sigma_{\tau-UPF}^2}. \quad (6.7)$$

The relative rms range and Doppler spread of the direct path were found to be 0.23 meters and 0.52 Hz., respectively. These values indicate that very little spread occurred in the direct path, which agrees with a visual comparison of Figures 6.9 and 6.11.

The surface bounce path spread may also be obtained by reregistering UP outputs relative to the surface path centroids. Figure 6.12 contains the 24 ping ensemble average of the reregistered surface bounce path arrivals, with the same contour levels as before. Clearly, a greater degree of spread is evident in the surface bounce path than in the direct path return. The rms spread in the surface bounce path relative to the UPF resolution was 1.97 meters in range and 9.98 Hz. in Doppler. At the time these measurements were made, the wind speed was 3.5 m/s, which corresponds to a sea state condition 2 [29]. This sea state would yield a rough surface, which could cause spreading in the surface reflections. The measured frequency spread is consistent with that predicted by the APL/UW model for this wind speed.

6.3.4 Receiver Performance

As shown in Chapter 4, the UP receiver is predicted to converge to its expected value at a rate of $1/\sqrt{N}$. Therefore, the convergence seen over 24 pings will not be as dramatic as that demonstrated in Chapter 4. However, if we compare the

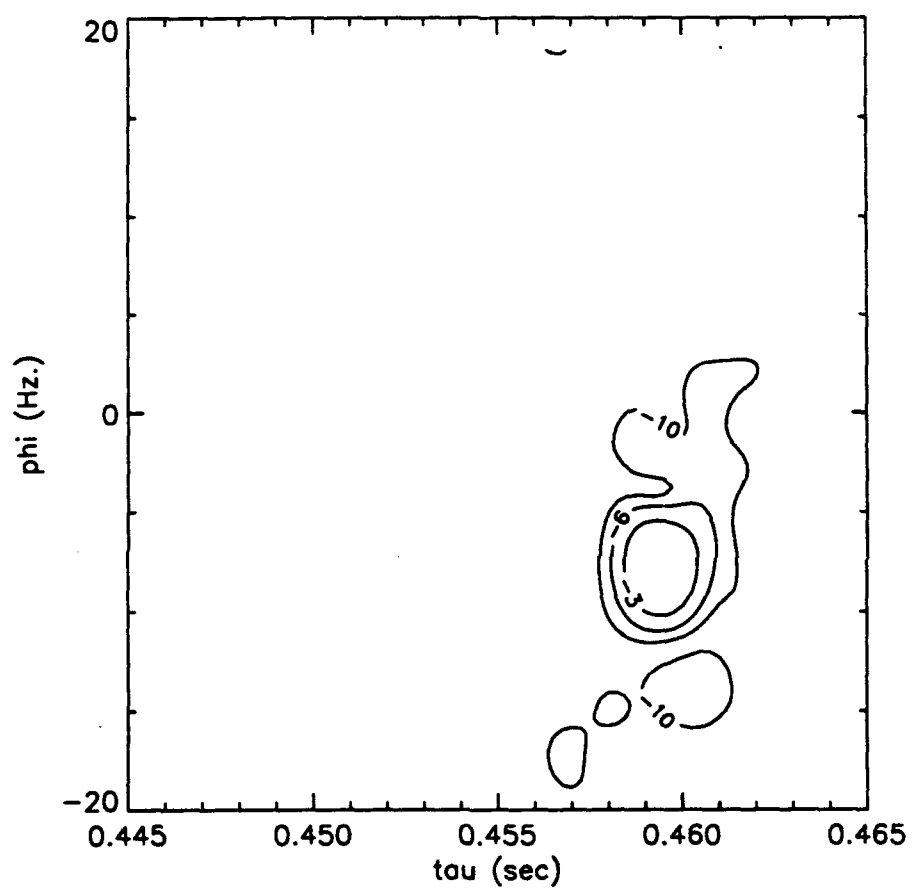


Figure 6.12: Surface Path Reregistered Uncertainty Product Receiver Ensemble Average

ensemble output of one of the matched filter receivers to that of the UP receiver, a distinct difference in background level should be seen. To form a proper comparison, matched filter outputs were reregistered relative to the direct path centroids prior to averaging. Figures 6.13 (a),(b) display the direct path reregistered ensemble outputs for the first waveform matched filter receiver and the UP receiver, respectively, as greyscale contours 3,6,10, and 16 dB down from the peak. Note the increased amount of self-clutter at the 10 and 16 dB levels for the matched filter in Figure 6.13 (a). The peak-to-background level for both matched filter ensembles of each channel and the UP ensemble are plotted as a function of the number of ensembles taken, in Figure 6.14. It appears from Figure 6.14 that, after 24 realizations of the scattering process, the UP receiver is converging to its expected value while the matched filter output has reached a steady state. The higher background level in the first channel matched filter output was caused by the higher sidelobes present in the truncated first waveform. Even though both receivers performed well due to the very high signal-to-noise ratio of the data, a significant advantage could be gained when using the UP receiver in situations where dense scattering induced self-clutter would normally mask the scattering function in the matched filter receiver.

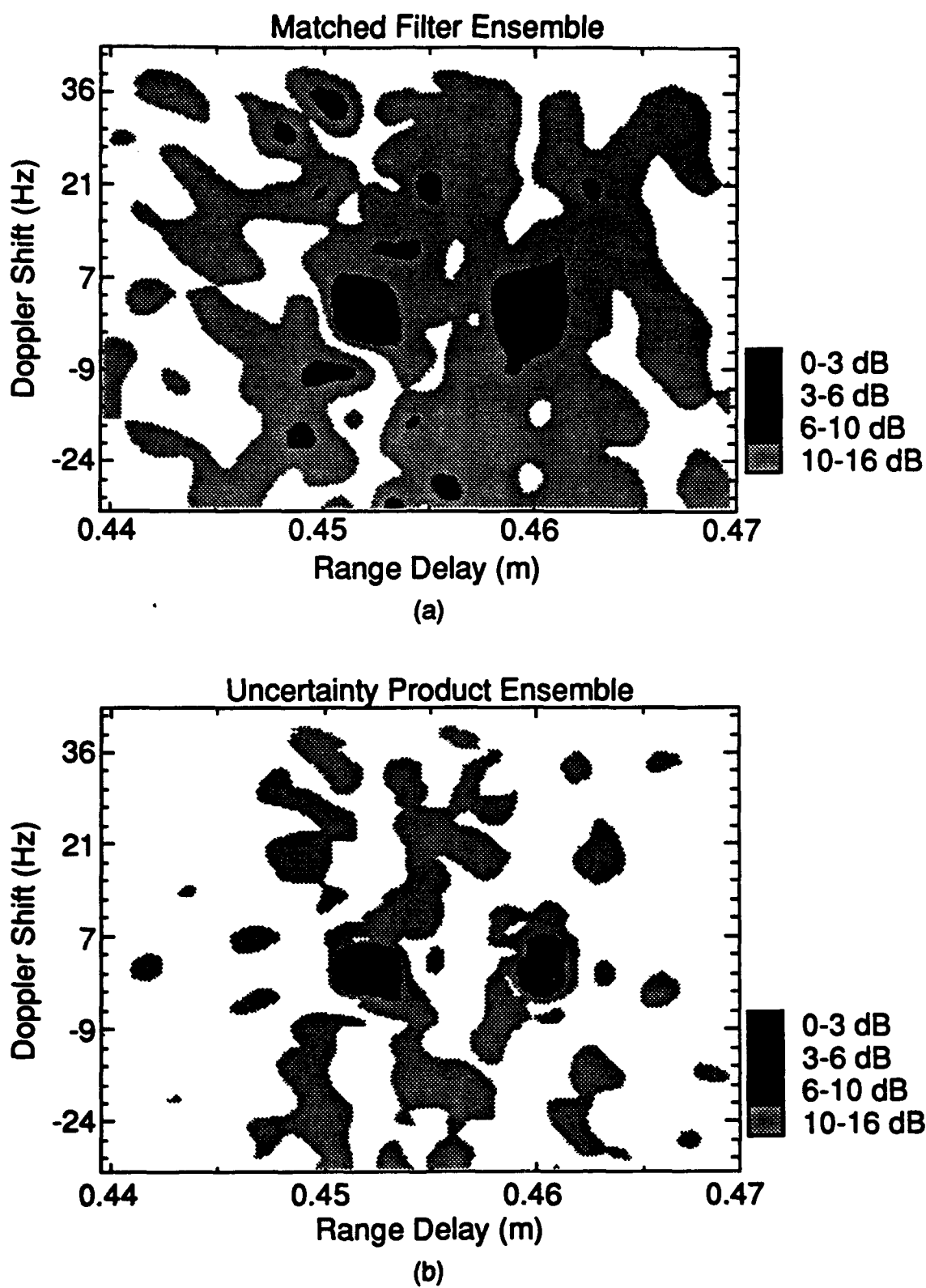


Figure 6.13: Receiver Ensemble Average Contour Maps

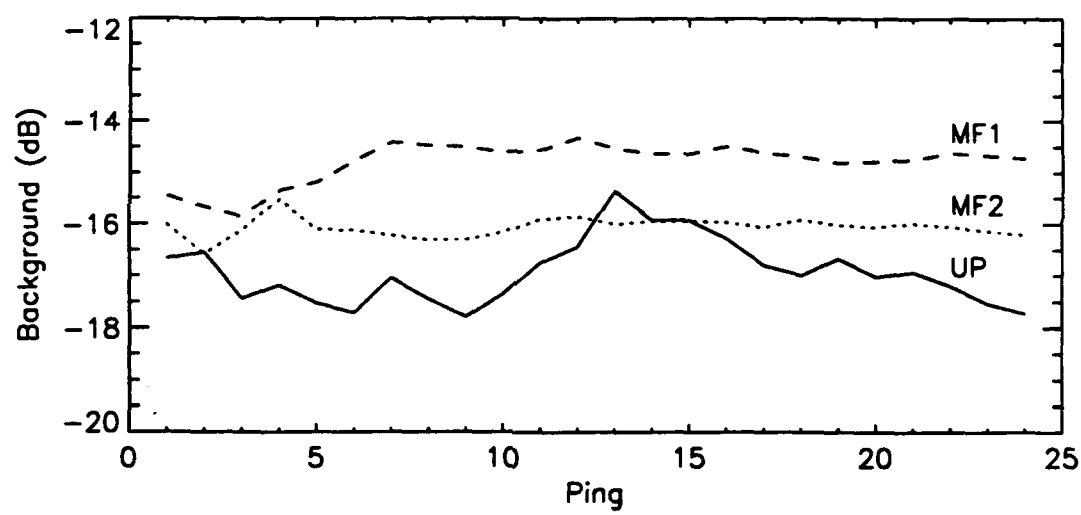


Figure 6.14: Receiver Convergence Comparison

Chapter 7

Summary and Conclusions

This thesis has presented the uncertainty product receiver as a method of estimating the structure of scattering phenomena in underwater communication channels. These channels were modeled as linear, time-variant, space-variant, random filters, and the time and frequency spreading of the channel was described in terms of this model. Next, the matched filter receiver was introduced and shown to be limited in the presence of dense scattering by self-clutter caused by its auto-ambiguity function pedestal.

The twin processor (or uncertainty product), as first proposed by Mehta and Titlebaum [1, 2], was introduced as a receiver structure which overcomes some of the limitations of the traditional matched filter receiver. Next, the uncertainty product function (UPF) was defined and used for determining UP receiver resolution and self-clutter suppression ability. Several properties of the UPF were developed, including the Fourier transform relationship between the UPF and the CAF. It was also noted that the expected value of the receiver can be written as the convolution of the scattering function with the UPF. This fact, and the property that the UPF does not have the volume conservation constraints of the ambiguity function, implies that the UP receiver is not subject to the limiting effects of self-clutter present in the matched filter and thus, is capable of producing better

estimates of the scattering process.

Although superior performance is expected with UP processing, several problems arise when two waveforms are used to interrogate the channel. These problems were illustrated using computer simulations and specifications for the clear area were developed to ensure that each signal interrogates the same realization of the scattering process, while minimizing the cross-ambiguity effects between the waveforms. The term "virtual scattering" was introduced to identify the interaction of the two uncertainty functions in the presence of two or more point scatterers. The rate of decay for the virtual scattering process was theoretically predicted and demonstrated via computer simulation.

Proper waveform selection was shown to be an essential issue in obtaining UP receiver performance. Waveform design techniques were reviewed and methods of selecting maximally resolvent and minimally interfering waveforms were presented. The hit array was shown to be a useful tool for determining both the UPF structure and the cross-ambiguity effects associated with hop code waveform pairs. The density of the scattering function being interrogated was shown to be the determining factor in waveform selection.

Finally, the results of using the UP receiver to measure open ocean channel scattering were presented. Forward surface scattering data was taken in the Pacific Ocean utilizing a dual hop code UP waveform to determine the performance of the UP receiver. Results from a 24 ping average matched filter and uncertainty product analysis of the data showed that the UP receiver is superior to the matched filter

at reducing self-clutter.

An extension of this work could include a study of the effects that slowly moving scattering processes have on the receiver. Additional work could involve the study of non-full hop codes or other waveform constructions not presented in this thesis. Also, methods of transmitting both waveforms simultaneously could be studied in order to reduce the effects of scatterer motion during the ping cycle. Finally, more in-water tests should be performed to obtain a larger data set for evaluating UP receiver performance. Ideally, these tests would involve both bistatic and monostatic geometries, where both the source and receiver are fixed or where ground truth position data is available for reregistration in the phase plane.

References

- [1] S. K. Mehta, E. L. Titlebaum, "A New Method for the Measurement of Target and Channel Scattering Functions using Costas Arrays and Other Frequency Hop Signals," *Proc. ICASSP*, Toronto, May 1991.
- [2] S. K. Mehta, "Signal Design Issues for the Wigner Distribution Function and a New Twin Processor for the Measurement of Target and/or Channel Structures," Ph.D. dissertation, University of Rochester (1991).
- [3] L. J. Ziomek, **Underwater Acoustics A Linear Systems Theory Approach** (Academic Press, Orlando, 1985), Sec. (5.2), pp. 176-188.
- [4] W. C. Knight, R. G. Pridham, S. M. Kay, "Digital Signal Processing for Sonar," *Proceedings of the IEEE*, Vol. 69, No. 11, November 1981, pp. 1451-1506.
- [5] L. J. Ziomek, L. H. Sibul, "Broadband and narrow-band signal-to-interference ratio expressions for a doubly spread target," *Journal of the Acoustical Society of America*, Vol. 72 (3), Sept. 1982, pp. 804-819.
- [6] H. L. Van Trees, **Detection, Estimation and Modulation Theory**, Vol. III (Wiley, New York, 1971), Chap. 13, pp. 444-557.
- [7] J. Bellagarda, E. L. Titlebaum, "The Hit Array: and Analysis Formalism for Multiple Access Frequency Hop Coding," *IEEE Transactions on Aerospace and Electrical Systems*, January 1991.
- [8] J. S. Bendat and A. G. Piersol, **Random Data Analysis and Measurement Procedures**, Second Addition, (John Wiley & Sons, New York, 1986).
- [9] N. T. Gaarder, "Scattering Function Estimation," *IEEE Transactions on Information Theory*, Vol. IT-14, No. 5, Sept. 1968, pp. 684-692.
- [10] D. M. Drumheller, D. W. Ricker, "Receiver-Transmitter Optimization for Detection in Doubly Spread Channels," *JASA*, Vol. 89, No. 4, April 1991, pp. 1714-1723.
- [11] C. E. Cook and M. Bernfeld, **Radar Signals an Introduction to Theory and Application** (New York, Academic Press, 1967), Chap. 4, pp. 59-108.
- [12] J. Costas, "A study of a class of detection waveforms having nearly ideal range-Doppler ambiguity properties," *Proceedings of the IEEE*, Vol. 72, August 1984, pp. 996-1009.
- [13] R. Price, E. M. Hofstetter, "Bounds of the Volume and Height Distributions of the Ambiguity Function," *IEEE Transactions on Information Theory*, April 1965, pp. 207-214.

- [14] S. W. Golomb, H. Taylor, "Construction and Properties of Costas Arrays," **Proceedings of the IEEE**, Vol. 72, No. 9, September 1984, pp. 1143-1163.
- [15] E. L. Titlebaum, "A Generalization of a Two-Dimensional Fourier Transform Property for Ambiguity Functions," **IEEE Transactions on Information Theory** (Correspondence), IT-12:80-81, January 1966.
- [16] E. J. Kelly, R. P. Wishner, "Matched-Filter Theory for High-Velocity, Accelerating Targets," **IEEE Transactions on Military Electronics**, Vol. MIL-9, No. 1, January 1965, pp. 56-78.
- [17] A. M. Mood, F. A. Graybill, and D. C. Boes, **Introduction to the Theory of Statistics**, third edition (McGraw-Hill, Inc. , New York, 1974), Chap. 6, pp. 233-236.
- [18] S. K. Mehta, E. L. Titlebaum, "The Product of Hit Arrays: A Tool for Code Design for Ambiguity Function Sidelobe Reduction," **Proc. of the Conference on Information Science and Systems**, John Hopkins University, March 1991.
- [19] F. J. Harris, "On the Use of Windows for Harmonic Analysis with the Discrete Fourier Transform," **Proceedings of the IEEE**, Vol. 66, No. 1, January 1978, pp. 51-83.
- [20] S. W. Golomb, H. Taylor, "Two-Dimensional Synchronization Patterns for Minimum Ambiguity," **IEEE Transactions on Information Theory**, Vol. IT-28, No. 4, July 1982, pp. 600-604.
- [21] E. L. Titlebaum, L. H. Sibul, "Time-Frequency HOP Signals Part II: Coding Based Upon Quadratic Congruences," **IEEE Transactions on Aerospace and Electronic Systems**, Vol. AES-17, No. 4, July 1981, pp. 494-500.
- [22] S. V. Maric, E. L. Titlebaum, "Two New Families of Frequency Hop Codes Based Upon the Theory of Congruences for Use in Multibeam Sonar Imaging," **IEEE Journal of Oceanic Engineering**, submitted.
- [23] D. W. Ricker, "A Logarithmic Frequency Allocation Algorithm for Wideband Discrete Frequency Pulse Trains," **IEEE Transactions on Aerospace and Electronic Systems**,(Correspondence), Vol. AES-18, No. 3, pp. 347-349.
- [24] E. L. Titlebaum, "Time-Frequency Hop Signals Part I: Coding Based Upon the Theory of Linear Congruences," **IEEE Transactions on Aerospace and Electronic Systems**, Vol. AES-17, No. 4, July 1981, pp. 490-493.
- [25] Correspondence between E. L. Titlebaum and D. W. Ricker.
- [26] R. J. Urick, **Principles of Underwater Sound**, Third Edition, (New York, McGraw-Hill, Inc., 1983), Chap. 6, pp. 193-197.

- [27] P. M. Morse, K. U. Ingard, **Theoretical Acoustics**, (Princeton University Press, 1986), Chap. 7, pp. 366-369.
- [28] Discussion with Peter Dahl of The Applied Physics Laboratory/University of Washington, 6 April 1993.
- [29] W. S. Burdic, **Underwater Acoustic System Analysis**, (New Jersey, Prentice-Hall, Inc., 1984), Chap. 5, pp. 130-133.